AN ABSTRACT OF THE THESIS OF

William Fairchild for the degree of Master of Science in Ocean, Earth, and Atmospheric Sciences presented on March 18, 2020.

Title: High-resolution Carbonate Dynamics of Netarts Bay, OR from 2014 - 2019

Abstract approved: _____

Burke Hales

Netarts Bay is a shallow, temperate, tidal lagoon located on the northern coast of Oregon and site of the Whiskey Creek Shellfish Hatchery (WCSH). Data collected with an automated flow-through system installed at WCSH capable of high-resolution (1 Hz) pCO_2 and hourly TCO_2 measurements, with measurement uncertainties of <2.0% and 0.5%, respectively, is analyzed over the 2014-2019 interval. These measurements provide total constraint on the carbonate system, allowing calculation of carbonate variables such as pH_t, alkalinity, and carbonate mineral saturation states. Nearly 70% of the bay's water is drained during each tide cycle, and in-bay fresh water sources are limited to small perennial streams or direct precipitation via high-rainfall events. Summer upwelling, wintertime downwelling, and in-situ bay biogeochemistry represent significant modes of the observed variability in carbonate dynamics. Summer upwelling is associated with large amplitude diel pCO_2 variability, elevated TCO_2 and alkalinity, but weak variability in salinity. Wintertime downwelling is associated with bay freshening by both local and remote sources, a strong tidal signature in salinity, TCO_2, and alkalinity, with diel pCO_2 variability

much less amplified when compared to summer. Further, analysis of alkalinity-salinity relationships suggests multiple and discrete water masses inhabiting the bay during one year: mixing of end-members associated with direct precipitation, coastal rivers, southward displacement of the Columbia River plume, California Current surface and deep upwelled waters. The importance of in-bay processes such as net community metabolism during intervals of high productivity are apparent. These direct measurements of pCO_2 and TCO_2 have proved useful to local hatchery owners who have monitored intake waters following historic seed-production failures related to high-CO_2 conditions exacerbated by ocean acidification. Continued monitoring efforts will produce baseline measurements necessary to understand how future warming and ocean acidification will impact our sensitive coastal environments.

High-resolution Carbonate Dynamics of Netarts Bay, OR from 2014-2019

by
William Fairchild

A THESIS

submitted to

Oregon State University

in partial fulfillment of
the requirements for the
degree of

Master of Science

Presented March 18, 2020
Commencement June 2020

Master of Science thesis of William Fairchild presented on March 18, 2020

APPROVED:

Major Professor, representing Ocean, Earth, and Atmospheric Sciences

Dean of the College of Earth, Ocean, and Atmospheric Sciences

Dean of the Graduate School

I understand that my thesis will become part of the permanent collection of Oregon State University libraries. My signature below authorizes release of my thesis to any reader upon request.

William Fairchild, Author

ACKNOWLEDGEMENTS

This project was only possible with the help and assistance of many kind and brilliant people, without whose help none of this would have been achievable.

First and foremost, I must thank my extraordinarily patient and infinitely knowledgeable advisor and mentor, Burke Hales. For two-and-a-half years he has challenged me to be a more critical thinker, a more cognizant and proficient scientist, and above all, a better person. The experience and knowledge I've gained from him is truly invaluable and will be carried with me for the rest of my life.

I must thank all the individuals at Whiskey Creek Shellfish Hatchery, Sue Cudd, Alan Barton, and the entire crew who makes the operation in Netarts Bay so incredibly successful. They have saved me many four-hour trips to-and-from Whiskey Creek by stepping in and changing a filter or removing a rogue mussel when they clog the flow.

Thank you to all of my friends and colleagues who have joined me in the frequently isolating weekly trips to Netarts—and of course their willingness to run check samples and help in the lab: Carrie Weekes, Selina Lambert, Michael Moses, Zoe Kilmer, Marnie Jo Zirbel, Sophia Wensman, Dale Hubbard, and of course Joe Jennings. Joe was there since day one to kindly and graciously teach me all the innerworkings of the lab space. His happy presence in the lab has been a constant source of warmth and generosity.

To all the faculty at CEOAS for their mentorship and guidance, they have made this experience a blessing: Maria Kavanaugh, Rick Colwell, Lori Hartline, Robert Allan, and George Waldbusser among many others.

Finally, I'm so grateful for my closest family and friends that have supported me emotionally and mentally during these past few years. Natasha—your humor, passion, uncompromising wit, and great friendship has kept me truly sane. David—our time together has been absolutely unreal I'm more thank thankful to have met you. My family,

mom, dad, Mckenna, Elyse, and Saman—the depth of your love continues to remain aberrant in this world and I'm so grateful for your unconditional support for me, I can only hope to return even a small fraction of it back. And, of course, my miraculous dog Zelda. Everyone said "don't get a dog in grad school, it's a bad idea." Well they were wrong.

TABLE OF CONTENTS

Page

Chapter 1 – Introduction 1

1.1 Context 1

1.2 Carbonate Chemistry 2

1.3 Historical CO_2 Monitoring 5

1.4 Project Objective 7

Chapter 2 – Netarts' Bay Carbonate Dynamics 8

2.1 Setting 8

2.2 Methods 10

2.2.1 Measurement approach 10

2.2.2 Calibrations and Standards 12

2.2.3 Servicing 13

2.2.4 Discrete Samples 14

2.2.5 Data QA/QC 14

2.2.6 Hybrid Alkalinity Model 14

3.1 Results 17

3.1.1 Summer 7-day basic observations 17

3.1.2 Winter 7-day basic observations 18

3.1.3 Summer 7-day derived observations 21

3.1.4 Winter 7-day derived observations 23

3.1.5 Single year basic observations 23

3.1.6 Single year derived observations 28

3.1.7 Composite year basic observations 28

3.1.8 Composite-year derived observations 29

4.1 Discussion 32

4.1.1 Timescales and Drivers of Variability 32

TABLE OF CONTENTS (continued)

Page

4.1.1.1 Diel Synchrony and Tide Phasing 32

4.1.1.2 Event-scale Variability 37

4.1.1.2 Seasonal Upwelling and Downwelling 39

4.1.2. Behavior of Alkalinity 40

4.1.2.1 Identifying Multiple End-Members 45

4.1.2.2 Metabolic-process Dominance 46

4.1.2.3 Hybrid Alkalinity Model 47

4.1.3 Implications for Ocean Acidification 50

4.1.3.1 Ocean Acidification Detection 50

4.1.3.2 Frequency of Low Omega Conditions 51

4.1.3.3 Anthropogenic CO_2 52

Future Work 56

Conclusion 56

Chapter 3 – Conclusions 58

Citations 61

LIST OF FIGURES

Figure Page

Figure 1. Map of the state of Oregon and satellite imagery of Netarts Bay. 8

Figure 2. Summer 7-day basic observations. 19

Figure 3. Winter 7-day basic observations. 20

Figure 4. Summer 7-day derived observations. 22

Figure 5. Winter 7-day derived observations 24

Figure 6. Composite-year basic observations. 25

Figure 7 Composite-year derived observations. 27

Figure 8. Composite-all years' basic observations 30

Figure 9. Composite-all years' derived observations. 31

Figure 10. Diel and tide phasing for summer. 33

Figure 11. Diel and tide phasing for winter 35

Figure 12. Wintertime event variability 38

Figure 13. Composite alkalinity-salinity regression 41

Figure 14. Comparison of regional alkalinity-salinity models 42

Figure 15. Alkalinity-salinity time-series for 2017 44

Figure 16. Hybrid alkalinity-salinity model output 48

Figure 17. Impact of anthropogenic carbon on *p*H and Ω_a. 53

Figure 18. Histogram representation of modern vs anthropogenic *p*H and Ω_a. 54

Figure 19. Check sample intercomparison. 72

Figure 20. Supplementary dissolved O_2 from 2019 73

LIST OF FIGURES (continued)

Figure Page

Figure 21. Representative raw xCO_2, salinity, and temperature for January 2019. 86

Figure 22. Non-QA/QCd TCO_2 response. 88

Figure 23. Raw xCO_2 pre-and-post masking 89

LIST OF TABLES

Table Page

1. ΔpH and $\Delta\Omega_a$ in relation to a fixed anthropogenic TCO_2……55

2. Output from a 24-hour piecewise linear alkalinity-salinity regression……69

3. Representative liquid standard calibration file……70

4. Representative gas standard calibration file……71

LIST OF APPENDICIES

Appendix Page

Appendix I. Regression output from the hybrid alkalinity-salinity mode 69

Appendix II. Liquid and gas standard calibration files 70

Appendix III. Check sample inter-comparison 72

Appendix IV. Supplemental dissolved oxygen data 73

Appendix V. Working Code 74

Appendix VI. Data processing 86

Appendix VII. Data access 90

Chapter 1 – Introduction

1.1 Context

Global levels of atmospheric carbon dioxide (CO_2) have risen 45% in the 200 years following the Industrial Revolution as a direct result of human fossil fuel combustion. At no time in the last 800,000 years have atmospheric CO_2 levels risen above the contemporary global level of 407 ppm, and this rate of increase has not been observed in approximately 420 million years (Foster et al., 2017). A climate perturbation of this magnitude has resulted in the oceans absorbing 36 billion metric tons of CO_2 emissions, or 40% of all anthropogenic carbon emissions since 1760 (Gruber et al., 2019; Reid et al., 2009). Therefore, it is of scientific interest to observe, model, and predict the biogeochemical, ecological, and physical transformations directly and indirectly related to climate change. Because even if global fossil fuel combustion ceased immediately, the earth would continue to warm 1.5° C by 2100 (IPCC, 2014).

Shallow coastal ecosystems, coral reefs, and temperate estuaries are among the most vulnerable oceanographic regimes threatened by exposure to elevated CO_2 and related anthropogenic forcing (Peirson et al., 2015). Enhanced nutrient loading from large-scale agricultural runoff, habitat loss, introduction of invasive species, altered freshwater flow, dredging, expanding 'dead zones' characterized by prolonged hypoxic episodes, and trace metal contamination represent some of the many stressors facing modern estuarine systems (Robert J. Diaz & Rosenberg, 2008a; Kennish, 2002). A warming planet has also reduced surface ocean oxygen saturation while enhancing stratification between warm

surface waters and cool, subsurface ocean water. In deep estuaries and fjord systems, this stratification enhances the frequency and duration of episodic hypoxia, defined as oxygen concentrations below 2.0 mg/L (R. J. Diaz & Rosenberg, 1995; Robert J. Diaz, 2001; Robert J. Diaz & Rosenberg, 2008b; N. N. Rabalais et al., 2009; Nancy N. Rabalais et al., 2002). Additionally, rising sea levels, ocean acidification, and loss of global marine biomass further complicate these vital ecosystems' health and stability and the goods and services they provide.

Studying and documenting how these environments are adapting and changing in response to environmental and anthropogenic stressors is vital if we wish to mitigate and preserve such sensitive and ecologically important habitats. Central to the question of how Earth's systems respond to increased greenhouse gases lies in understanding marine carbonate chemistry.

1.2 Carbonate Chemistry

The marine carbonate system is a dynamic series of biogeochemical reactions occurring at highly variable time and space scales. Dissolved inorganic carbon exists in three primary inorganic forms: aqueous dissolved CO_2 ($[CO_2(aq)]$), bicarbonate ($[HCO_3^-]$), and carbonate ($[CO_3^{2-}]$) with a minor form of aqueous CO_2 ($[H_2CO_3]$) existing in fleetingly negligible quantities. The sum of all inorganic species is termed TCO_2—total dissolved inorganic carbon dioxide; sometimes cited in literature as DIC (England et al., 2011; Zeebe, 2012). Fundamentally, the balance between $[HCO_3^-]$, $[CO_3^{2-}]$, and $[CO_2^*]$ which represents ($[CO_2(aq)] + [H_2CO_3]$), forms the basis of the marine carbonate system and the method by which the ocean buffers acid-base perturbations.

The relative proportion of these three inorganic carbon species is dictated by well-known thermodynamic relationships dependent on temperature, pressure, and salinity. For the modern ocean, 90% of all inorganic carbon species exists as bicarbonate, with ~8% carbonate, and ~2% carbonic acid, resulting in an average pH_t ~8.1.

pCO_2, the partial pressure of carbon dioxide in seawater, is a property of seawater that can be determined by equilibrating headspace gas with a liquid sample using a spray head or soaker hose in a tightly sealed equilibration chamber until completely equilibrated. On the other hand, TCO_2 is routinely measured by adding enough acid (HCl) to convert all species into CO_2^*, evolving the gas from the liquid phase, and measuring it via infrared detection.

An essential parameter used to constrain the carbonate system is total alkalinity (TA) which is defined as the buffering capacity of a solution's conjugate bases to its weak acids (Waldbusser & Salisbury, 2014; Zeebe, 2012). Weathering reactions of continental rock and subsequent riverine delivery of carbonate and bicarbonate ions to ocean margins, as well as carbonate shell formation and dissolution in the water column are the primary drivers that change global ocean alkalinity (Zeebe, 2012). Alkalinity is a conservative property unaffected by changes in temperature, pressure, and importantly gas exchange, and thus serves as a useful tracer to identify source waters within the oceans. However, within shallow coastal environments and estuarine systems which have close benthic-pelagic biogeochemical coupling, and through various oxic and suboxic metabolic, and local dilution/mixing processes, alkalinity can behave non-conservatively with respect to

salinity (Howland et al., 2000). For large areas of the ocean, such as oligotrophic gyres, changes in alkalinity are largely covariant with changes in salinity.

Another historically useful metric for tracking changes in marine habitat stability and biogeochemical perturbations to the ocean is the measurement of pH_t, defined as the negative log of the hydrogen ion concentration ($[H^+]$). Upon gaseous CO_2 invasion, whether it be through direct atmospheric gas exchange or biological respiration, CO_2 undergoes rapid hydrolysis and dissociation into subsequent carbonate species raising the relative abundance of hydrogen ion, therefore lowering pH_t. In the last 100 years, global ocean pH_t has declined 0.1 units, corresponding to a 30% increase in proton concentration (Gattuso et al., 1998) in response to absorbing anthropogenic atmospheric CO_2—this is the process termed ocean acidification.

Ocean acidification critically alters the availability of carbonate ions and the integrity of biominerals such as calcite and aragonite ($CaCO_3$). Calcifying organisms such as coccolithophores, pteropods, and shellfish take in dissolved carbonate and calcium ions to form exoskeletal structures (Eq. 1). A useful metric among oceanographers is the mineral saturation state of calcium carbonate, Ω, which relates the concentration of calcium and carbonate ions to the apparent solubility (K'_{sp}) product in seawater (Eq. 2):

$$Ca^{2+} + CO_3^{2-} \leftrightarrow CaCO_3 \qquad \text{(Eq. 1)}$$

$$\Omega = \frac{[Ca^{2+}][CO_3^{2-}]}{K'_{sp}} \qquad \text{(Eq. 2)}$$

As seawater becomes more acidic, the equilibrium of inorganic carbon species begins to shift in such a way that lowers the abundance of carbonate ions, thus lowering Ω.

Laboratory studies suggest that the saturation state is an important indicator of larval shellfish success and that exposure to low saturation state waters, particularly in the first 48 hours of development is a determining factor in survivability (Barton et al., 2012; Waldbusser et al., 2015). Below a saturation state of 1.0 and the system thermodynamically favors dissolution of mineral calcium carbonate back into solution.

The global surface ocean is expected to continue acidifying as atmospheric CO_2 rise, with estimates of pH_t 0.3-0.4 units less than modern values by the end of the century. Correspondingly, the global ocean margins will be largely undersaturated with respect to calcium carbonate by the year 2100 (Gattuso & Hansson, 2011)

1.3 Historical CO_2 Monitoring

Near-shore monitoring studies of oceanic CO_2 in the Pacific Northwest have primarily been limited to shipboard measurements in tandem with buoy observations during upwelling intervals (Evans et al., 2011; Feely et al., 2008; van Geen et al., 2000; Ianson et al., 2003; Nemcek et al., 2008) while more recent work of the Columbia River, Puget Sound, and Salish Sea have introduced CO_2 data at higher spatiotemporal resolution (Evans et al., 2013, 2019). The lack of extensive spatiotemporal sampling represents a hurdle in understanding how the dynamic coastal ocean and estuarine environments are interacting with and responding to the cascading and complex problems associated with

ongoing climate change. Biophysical processes within shallow coastal shelves and estuarine bodies occur across variable time and space scales (Waldbusser & Salisbury, 2014), from hours to interannual, and forecasting how these environments will respond to climate change has proved challenging, requiring more expansive and higher resolution coastal monitoring networks.

Despite poor data coverage, our understanding of ocean acidification's impact on organismal life cycles, specifically for larval and juvenile bivalves, shows these organisms experiencing physiological stress across varying levels of pCO_2, pH_t, and/or saturation state at levels currently observed during various periods of the year (Barton et al., 2012; Waldbusser et al., 2011; Waldbusser, Hales et al., 2015; White et al., 2013). Ocean acidification-related symptoms include, but are not limited to, compromised shell integrity, increased mortality, and reduced recruitment success. *Crassostrea gigas*, for example, shows enhanced sensitivity to water conditions during the first 48 hours of calcification (Barton et al., 2012). An under sampling of the coastal ocean in both time and space may result in these bivalve-poor water conditions to be overlooked entirely.

However, it does not necessarily take high-resolution carbonate sampling to understand in real-time how ocean acidification is threatening habitat stability, organismal life cycles, and even fisheries economies. During the summer of 2009, Whiskey Creek Shellfish Hatchery in Netarts Bay, OR, sustained significant and prolonged larval oyster mortality in response to intake water which proved corrosive and fatal to their broodstock (Barton et al., 2012). Real-time liquid flow-through pCO_2/TCO_2 instrument was installed in 2011 to monitor in-take water conditions. Coincident with water chemistry

monitoring, hatchery operators moved the growing season to earlier in the year and began conditioning incoming seawater with a slurry of sodium carbonate to elevate saturation states to optimal shellfish growing levels. In an industry worth $270 million regionally and one which employs 3000+ people (fisheries.noaa.gov), implementation of this strategy to mitigate the severe effects of ocean acidification on bivalve mortality has been beneficial for hatchery operators at Whiskey Creek. Recreational shellfishing, on the other hand, will be more directly impacted by changing ocean carbonate chemistry since the intertidal zone and shallow estuarine shellfish habitats are directly exposed to dynamic carbonate conditions.

1.4 Project Objective

I analyzed a 6-year, high-resolution record of in-situ pCO_2, temperature, salinity, hourly TCO_2, alkalinity, pH_t, and aragonite saturation state for Netarts Bay, Oregon. During the 2008-2009 shellfish growing season, shellfish hatchery operators and private growers experienced unusually high larval mortality throughout the Pacific Northwest region which was later directly linked to ocean acidification. This research and continued monitoring efforts will provide insight into the daily, seasonal, and annual carbonate trends that may not be captured by discrete sampling measures.

Chapter 2 – Netarts' Bay Carbonate Dynamics

2.1 Setting

Netarts Bay is a temperate, well-mixed, tidal lagoon located 90km south of the Columbia River mouth on the Oregon Pacific coast (Figure 1). Two basaltic headlands, Cape Meares to the north and Cape Lookout to the south, bound the estuary (Mulder, 2000). A 6km-long sandspit stretching north-to-south forms the seaward boundary of the estuary. The primary exchange of water occurs at the ~100m wide tidal channel located at the northern end of the spit.

Figure 1. Map of the state of Oregon (right) and satellite imagery of Netarts Bay (left), red X marks site of Whiskey Creek Shellfish Hatchery (WCSH). Images courtesy of Google Earth.

Of the 22 major estuaries in Oregon, Netarts Bay is the 6th largest (by area) with a surface area of 941 Ha, 612 of which are tideland and 329 being permanently submerged (McCallum, 2000). Draining a 4100 Ha watershed, the bay is marine-dominated, receiving freshwater input only from about a dozen very small streams, primarily during the winter storm seasons (McCallum, 2000). The temperate climate of Netarts Bay is characterized by cool, wet winters and dry summers, with typical annual precipitation amounts averaging 228 cm, primarily during the months of November through March. Average daily air temperatures can range from 0-10°C in winter to 15-25°C during summer.

The bay is heavily influenced by mixed semidiurnal tides with a maximum tidal range of 3m, which is similar to the bay's average water depth. The tidal prism between mean low water and mean high water is 9.4x10^{6} m^{3}. The net effect of bay hydrology and tidal dynamics results in rapid flushing and water residence times <12 hours (Glanzman, 1971). A single ebb-flood cycle can replace nearly 70% of the bay's water during intervals of spring tides (Glanzman, 1971). Dye studies conducted by the USGS indicate that the bay is vertically well-mixed and experiences no density stratification (Shirzad, 1988)

Water moves through the bay by means of branching tendrils connected to one central channel approximately 8m deep. This central artery drains into the Pacific Ocean at the mouth of the bay during ebb tide, often resulting in most of the mudflats and salt marshes completely exposed to the atmosphere while permanent subtidal zones remain limited to the deepest central channels. *Zostera spp.* beds cover roughly 2/3 of the silty tidal flats while saltwater marshes cover much of the southern end (Glanzman, 1971).

Roughly 72 epiphytic and sediment-associated diatoms recorded within the adjacent shoreline have been documented in the bay (Whiting & McIntire, 1985).

Less than 1000 people live within the watershed, a majority of whom inhabit the eastern banks. A few oyster farms line the eastern shoreline of the bay while mudflat shellfishing represents the primary outlet of recreational activities. The watershed is impacted mostly by commercial forestry (65% by area) and less so by agriculture (2% by area) (McCallum, 2000). The Oregon state land-use program has classified Netarts Bay as a Conservation Estuary which limits industry and promotes and protects sensitive ecological habitats such as eelgrass beds.

2.2 Methods

2.2.1 Measurement approach

Whiskey Creek Shellfish Hatchery (WCSH; 45.403°N, 123.944°W) is located on the eastern bank of Netarts Bay, approximately 2 km south of the bay's mouth (Figure 1, red X). Operating year round, the hatchery pumps in seawater through an intake pipe which remains submerged below the water line during all tide stages. This water is pumped throughout the facility and used to fill large tanks for shellfish seed production. During the 2007-2008 growing season, hatcheries up and down the Pacific Northwest coast, including WCSH, experienced intermittent but significant mass larval mortality, which was later directly linked to high-CO_2 content in intake waters (Barton et al., 2012, 2015). Beginning in 2011, Vance (2012) installed an automated system that combined pCO_2 and TCO_2 measurements, following the TCO_2 system as described by Bandstra et al. (2006)

combined with the pCO_2 system described by Hales et al. (2004) modified to use a showerhead-style equilibrator. This precursor system was redesigned prior to 2014 and has been in operation more or less continuously in its current configuration since then.

Briefly, intake water is branched into an adjacent side-laboratory, passing through a coarse screen, and then through a SeaBird Electronics 45 MicroTSG which continuously measures in-situ temperature and conductivity, allowing determination of salinity. Downstream of the TSG is an enclosed-headspace shower-head equilibrator in which the seawater flows over a porous bubbler tube where the recirculated headspace gas is introduced to the equilibration chamber. High water flow rates and vigorous bubbling ensures complete equilibration of the headspace gas CO_2 with the dissolved CO_2 in the sample stream. The headspace gas is recirculated in a closed loop, passing through an detector unit (LI-COR 840; licor.com), where the CO_2 content of the gas is measured via infrared.

Once an hour, the instrument performs a TCO_2 sequence closely following the method of Bandstra et al. (2006). Water is drawn from the main seawater flow through a custom 40-micron tangential-flow filter at a pump-controlled 20 mL/min and acidified with a 0.1 mL/min flow of a solution of 30% concentrated HCl in distilled water. The acidified liquid sample stream flows through the lumen-side of a hydrophobic microporous membrane contactor, while a CO_2-free gas stream controlled at 900ml/min flows counter to the liquid stream on the shell-side of the contactor. A steady-state mass balance governs the CO_2 composition of the outlet gas stream. With precisely controlled

gas and liquid flows, the xCO_2 of the effluent gas stream, measured by the LI-840, is proportional to the TCO_2 of the sample water.

The instrument is controlled by a computer and a custom acquisition and control program developed in LabView. Basic data (LI-840, mass flow, and SBE45 output, and several operational analog sensors) is sampled and stored at 1-Hz frequency. At user-specified intervals (30 seconds here), the program calculates medians of the continuous data, applies calibrations and corrections, and performs carbonate-system calculations to give real-time estimates of water pH_t and mineral saturation states.

2.2.2 Calibrations and Standards

The system automatically runs both gas and liquid-phase standards at user-specified intervals (6 hours for this work) to verify detector accuracy and the relationship between TCO_2 outlet strip gas and inlet-water TCO_2 concentration. Gas standards are a set of three cylinders of gravimetrically prepared mixtures of CO_2 in ultrapure air, typically spanning the range of 200-2000 ppm, but there were variations over the course of this study. The LI-840 is linearized over a range of 0-20000 ppm, and we have verified this linearity up to 7000 ppm in the laboratory. In the instances where the natural dynamic range exceeds the calibration range, we are confident that our linear regression (R^2 typically > 0.999, n=3) can be extended to any CO_2 level observed here. Liquid standards are three solutions of $NaHCO_3$ and Na_2CO_3 in deionized water, in proportions selected to maintain near-ambient solution pCO_2 at TCO_2 concentrations of 1200, 1800, and 2400 µmol/kg. The liquid calibration is likewise highly linear (R^2 typically > 0.99, n=3).

Calibration sequences are processed, and regressions performed in real time. At each calibration interval, measurements of outside air xCO_2 and barometric pressure are made.

To cross-check the accuracy of the instrument's TCO_2 response, certified reference materials (CRM) provided by Scripps have been run intermittently during the past several years. These CRMs contain highly accurate and precisely known concentrations of TCO_2 and alkalinity. On-site TCO_2 measurements of these CRM's consistently produce correction factors 0.985 ± 0.005, so we applied a single correction of 0.985 to our TCO_2 data over the duration of the study. This implies an uncertainty of ±0.5% (~10 μmol/kg) in TCO_2, which exceeds that achievable in a more controlled operation (Bandstra et al., 2006), but is quite small in the context of this dynamic setting.

2.2.3 Servicing

Approximately once a week, the WCSH laboratory undergoes routine maintenance. Biofouling of the pipes can reduce liquid flow-through, at worst obstructing flow completely. Using a submerged pump and a 5-gallon bucket, fresh water is rinsed through the pipes, followed by an acid/bleach/acid rinse sequence and a final freshwater rinse. Bioaccumulation within the equilibration chamber can block airflow through the porous bubbler tube and thus interfere with sample collection; physically scrubbing the hose and the interior of the chamber is sometimes necessary for optimal performance. Additionally, an aerosol inlet filter used as the final prevention of direct water contact in the LI-840 is replaced once a week. Biofouling is a constant issue at WCSH but varies with season and adjacent coastal ocean conditions.

2.2.4 Discrete Samples

During routine servicing, grab samples are collected before and after cleaning. Samples are collected in 350ml amber glass bottles downstream of the equilibration chamber, poisoned with mercuric chloride, and capped with metal bottle caps. These samples are analyzed in the Hales laboratory at Oregon State University using combined pCO_2/TCO_2 measurements as described above but modified for discrete samples. Check samples reveal that pCO_2 measurements at WCSH are within 5% of the discrete-sampler system, while TCO_2 measurements are within 1-2% (See Appendix III). Discrepancies between the two measurements can arise from human error such as inconsistent sampling procedure, failure to adequately poison the discrete sample bottle, and occasional transcription errors.

2.2.5 Data QA/QC

Six years of high-resolution (1Hz) data are presented in this paper. Raw xCO_2 measurements are corrected for using the linear regressions performed from bracketing gas standard sequences. Experiments by Vance (2012) and personal experiments at the OSU lab indicate that instrument drift is likely linear through reasonably short timescales (e.g. days), therefore any observed difference between two gas standard sequences is assumed to have occurred linearly between the time of each standardization sequence. A drift correction is applied to the converted data using a linear interpolation in time. $xTCO_2$ data are likewise converted using the set of liquid standard sequences which bookend any given TCO_2 measurement. A density and CRM correction are applied post-conversion to

arrive at units of μmol/kg. Synchronizing hourly TCO_2 measurements with temperature, salinity, and time-weighted interpolated pCO2 value allows for calculation of hourly alkalinity, pH_t and mineral saturation with use of a program such as CO2Sys or CarbCalc, though we use our own calculation program here. Full data processing was accomplished using compiled language and programs written in RStudio (version 1.2.5033; see Appendix IV for more detail).

Further QA/QC was applied manually to remove instances of system malfunction (See Appendix VI for details). Such instances included times of seawater flow stoppage, either in the main hatchery supply or in the branch to the laboratory, clogs in the headspace recirculation airflow, LI840 detector failures, HCl depletion, etc. These failures were recognizable from anomalous system variables, such as flow or pressure readings, atypical temperature and salinity readings, among others.

2.2.6 Hybrid Alkalinity Model

We developed a hybrid alkalinity model to resolve carbonate chemistry at the high-resolution of the pCO_2 data product because there is observed sub-hourly variability occurring for both measured pCO_2, temperature, and salinity. For most of the open surface ocean, alkalinity-salinity variability is highly linear, with large oceanic sub-regions characterized by well-known alkalinity-salinity relationships (Takahashi et al., 2014). However, in estuarine systems which have strong benthic-pelagic metabolic coupling and variable freshwater endmembers, a single alkalinity-salinity relationship is not useful to describe the various mixing curves observed over a year. As discussed below, Netarts Bay

has multiple freshwater endmembers and an apparent summertime metabolically-influenced alkalinity characteristic that is non-linear with respect to salinity.

In order to capture sub-hourly carbonate chemistry, we took advantage of the highly linear alkalinity-salinity relationships during the winter months and created a forward-moving piecewise linear regression model. We first combine hourly TCO_2 values with a time-interpolated pCO_2 value paired with temperature and salinity to calculate hourly alkalinity. The moving regression calculates slope, intercept, R^2, slope and intercept deviations, and average absolute deviation. To account for measurement uncertainties in both alkalinity (~10 μeq/kg) and salinity (~0.01), we used a least squares bisector calculation (Equations from Bevington & Robinson, 1992) which finds the slope of the line that bisects the minor angle between the regression of Y-on-X and X-on-Y. We use a minimum of 6 points (6 hours) wherein salinity variability is at least 0.25, perform the regression, and omit data based on a set of criteria. Regressions with R^2 less than 0.7 are rejected. Slopes and intercepts calculated in the thousands and/or large negative slopes and intercepts are rejected even when R^2 is greater than 0.7 are also rejected—these large slopes and intercepts are not geochemically realistic. The model moves forward through hourly alkalinity calculations to provide piecewise regression statistics. Using a basic point-slope formula, alkalinity is calculated from measured salinity. pH_t, TCO_2, and Ω_a are calculated from the paired high-resolution alkalinity, pCO_2, temperature, and salinity.

For the summertime when the forward-moving piecewise regression fails, we perform a simple time-interpolation of hourly alkalinity at the resolution of pCO_2.

Combined is the hybrid alkalinity model which resolved carbonate chemistry between hourly TCO_2 analysis

3.1 Results

The time series data presented below represent a highly dynamic system, with multiple timescales of variability. Our examination of the data revealed four key timescales of variability: diel, which persists throughout the year; seasonal, reflecting the transition between predominantly-upwelling summer and predominantly-downwelling winter conditions; summer-event variability associated with upwelling/relaxation cycles; and winter-event variability associated with storms and precipitation events. There are other scales of variability present, such as sub-hourly, but our discussion will focus on elucidating those listed above, using the data from 2017 as exemplary in terms of data coverage before presenting the 2014-2019 composite.

3.1.1 Summer 7-day basic observations

Representative plots of the measurements of summertime temperature, salinity, and pCO_2 at 30-second resolution, and TCO_2 at hourly resolution for a 7-day period in June of 2017 (day-of-year 169-176) are shown in Figure 2. For reference the modeled tide height is shown as a spline-fit of daily high-and-low tides (data courtesy of https://tidesandcurrents.noaa.gov/), and shading represents local day- and night-time. In-bay temperature ranges between 14°C and 17.5°C with little systematic variability from day-of-year 169-173 until decreasing in temperature but growing in tidal variability from day

173-176. Salinity experiences variability more closely synchronized with the local tide stage, initially varying between 26.2-28 until day 173, when salinity increases to 33.5 and remains high through day 176. pCO_2 shows strong diel variability from <200 µatm to >800 µatm in this interval. pCO_2 tends to increase during the night hours, peaking either immediately before or shortly after sunrise, and then rapidly fall throughout the day, reaching daily minima in late afternoon or early evening.

Early in the observation period, TCO_2 shows clear pCO_2-synchronous diel variability with dawn maxima around 1900 µmol/kg and late afternoon minima around 1700 µmol/kg, until late in day 173, when TCO_2 shows a large increase (~150 µmol/kg) coinciding with the step up in salinity. Following day 173, TCO_2 continues to show diel variability with morning maxima slightly over 2100 µmol/kg and evening minima slightly under 2000 µmol/kg.

3.1.2 Winter 7-day basic observations

Corresponding representative plots of a seven-day interval in February of 2017 (day-of-year 48-55) are shown in Figure 3. Temperature varies weakly between 9.4°C and 11.2°C without obvious diel or tidal character. Salinity varies strongly between 26 and 31, with a clear tidal covariance. pCO_2 ranges between 325 – 420 µatm with evident diel amplitude, but with a dramatically smaller dynamic range than seen in the summer. The

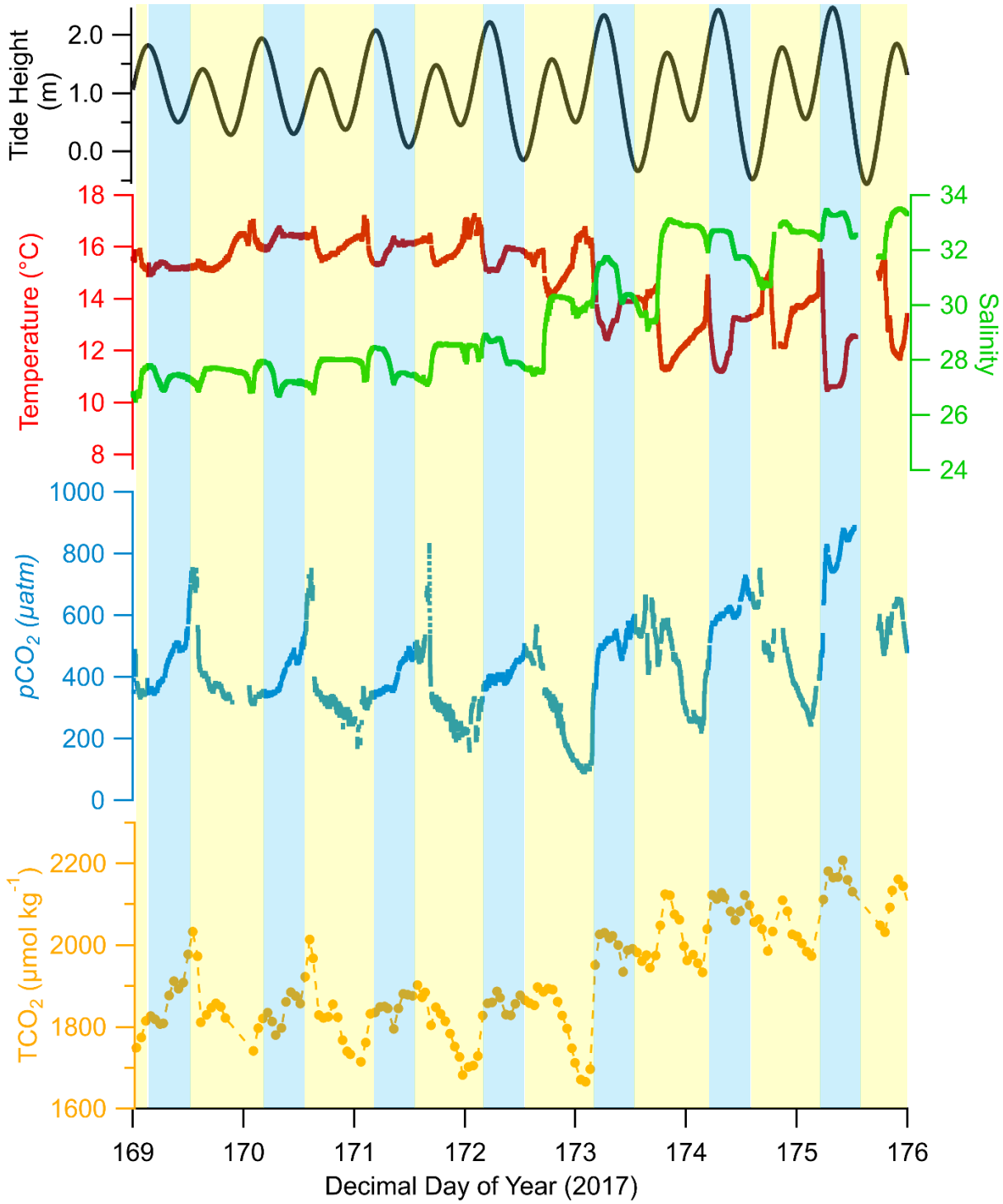

Figure 2. 7-day period summer 2017 for Netarts Bay. Temperature (red line), salinity (green line), pCO_2 (blue line), TCO_2 (orange dots connected by dashed line), and estimated tide height (black line) for 7 days during a summer period, 2017, at Netarts Bay, OR. Blue shading indicates local nighttime and yellow shading indicates daytime.

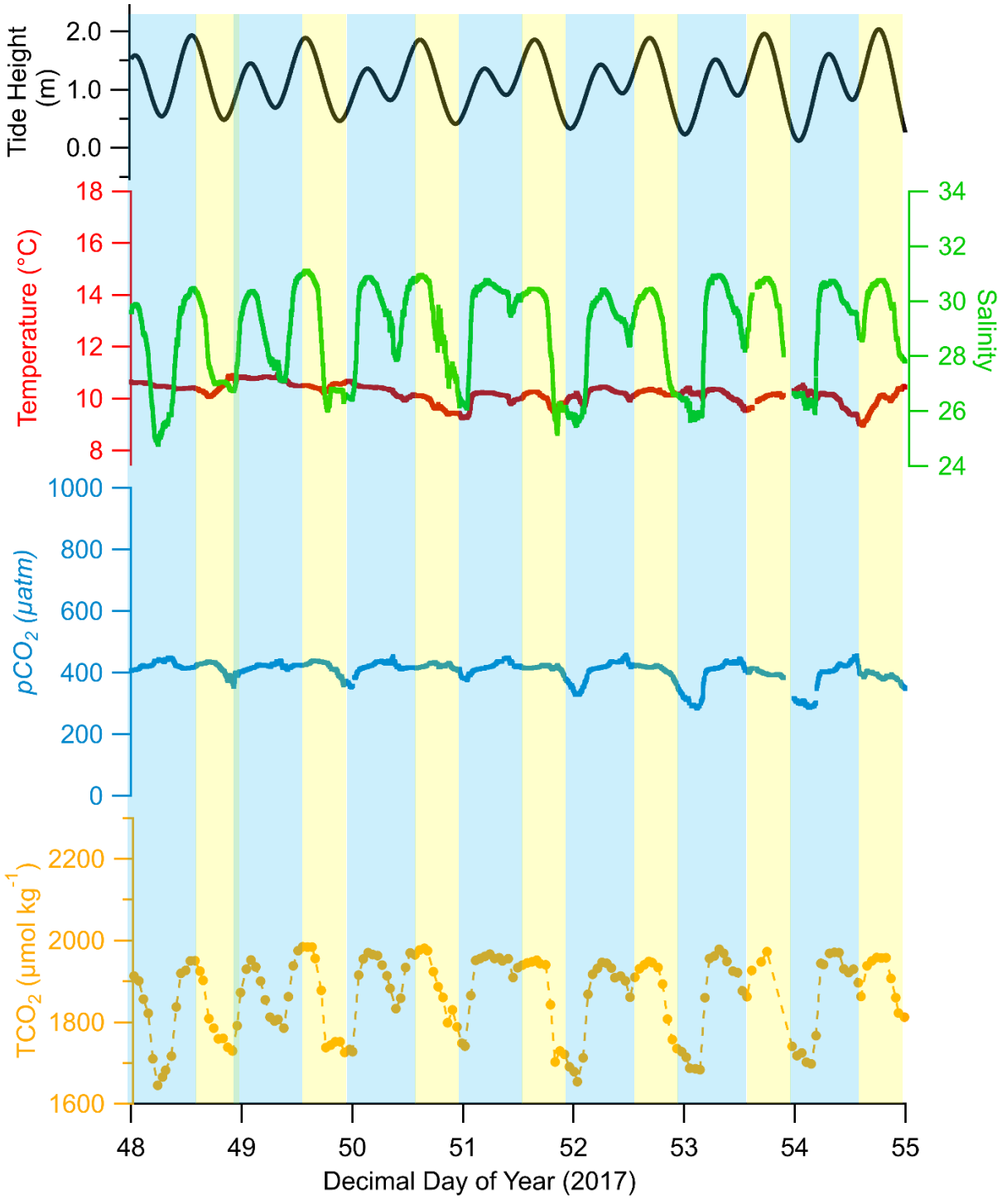

Figure 3. 7-day period winter 2017 for Netarts Bay. Temperature (red line), salinity (green line), pCO_2 (blue line), TCO_2 (orange dots connected by dashed line), and estimated tide height (black line) for 7 days during a winter period, 2017, at Netarts Bay, OR. Blue shading indicates local nighttime and yellow shading indicates daytime.

overall trend of decreasing pCO_2 throughout the afternoon and build-up throughout nighttime persists of decreasing pCO_2 throughout the afternoon and build-up throughout nighttime persists in winter. TCO_2 ranges from 1620 – 2000 µmol/kg, large compared to the summer observations. That variability is largely positively correlated to salinity for this period, with diel variability and pCO_2 co-variance less evident than seen in summer.

3.1.3 Summer 7-day derived observations

As discussed in the methods section, hourly TCO_2 measurements are combined with a synchronized, time-interpolated pCO_2 value to calculate hourly alkalinity, pH_t, saturation state, and a series of other carbonate variables including individual inorganic carbon species as determined through thermodynamic relationships. Figure 4 adds alkalinity, pH_t, and the saturation state of aragonite (Ω_a) to the basic T, S, pCO_2 and TCO_2 observations for the 7-day summer interval of Figure 3. Alkalinity is largely covariant with the TCO_2 data in the first 4 days of the interval, varying from 1900 – 2100 µmol/kg. In the final three days, alkalinity increases with the step up in salinity, and then has only minimal variability between 2100-2150 µmol/kg for the remainder of the record. pH_t behavior is primarily anti-correlated with the pCO_2 observations, showing the diel pattern of lowest values ~7.8 in the early morning, and highest values, ~8.1 or higher, in late afternoon or early evening. The saturation state ranges from 1.0 to over 4.6 in similar diel cycling as the pH_t values, and

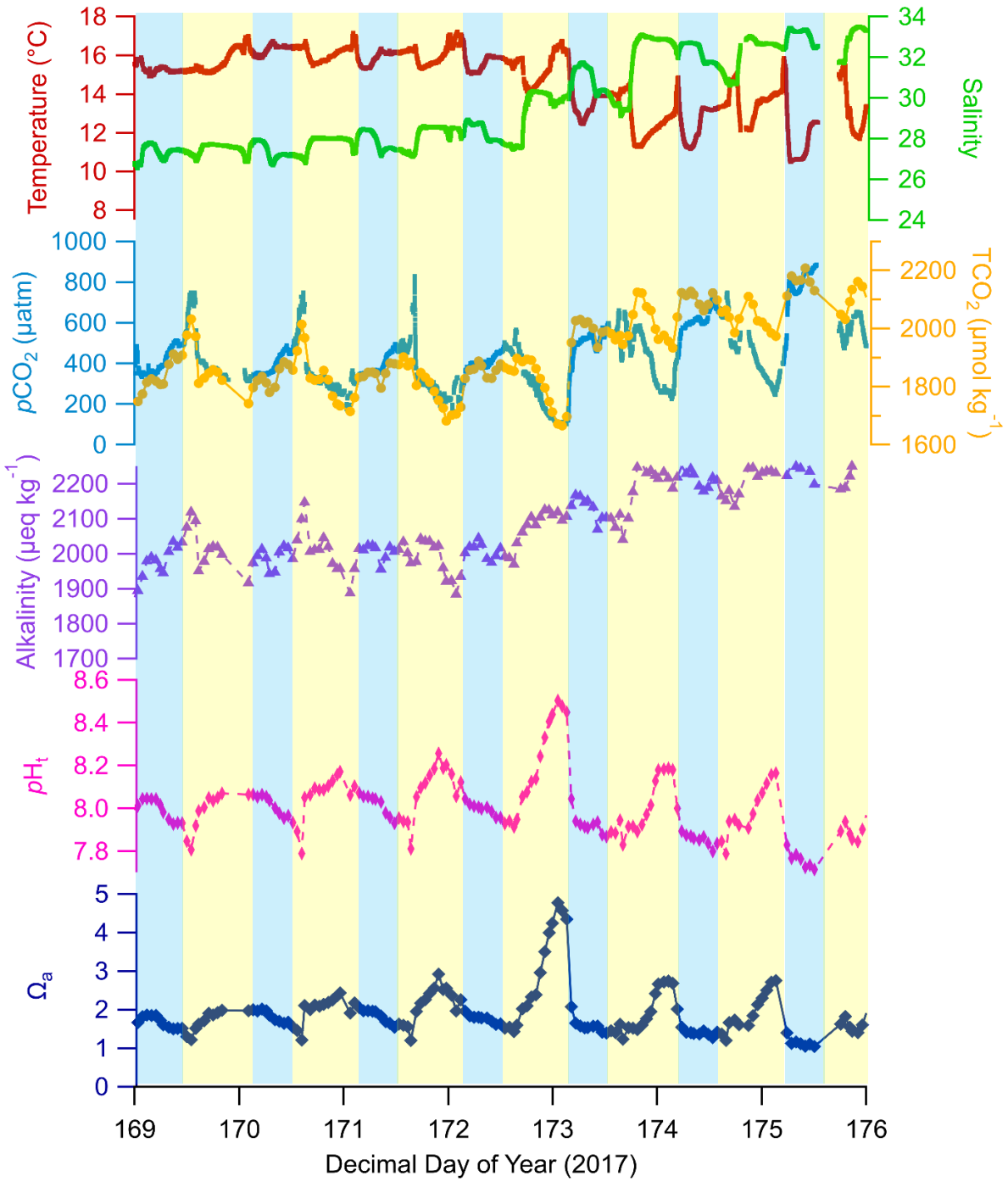

Figure 4. 7-day period summer 2017 for Netarts Bay. pCO_2 (blue line), TCO_2 (orange dots connected by dashed line), and calculated alkalinity (purple triangles connected by dashed line), pH (pink stars diamonds by dashed line),and saturation state of aragonite (Ω, blue squares connected by dashed line) for 7 days during a summer period, 2017, at Netarts Bay, OR. Blue shading indicates local nighttime and yellow shading indicates daytime.

thus anti-correlated with in-situ pCO_2, with lowest saturation states in late-evening or early morning, and highest values in late afternoon.

3.1.4 Winter 7-day derived observations

Figure 5 shows the corresponding wintertime-interval alkalinity, pH_t, and Ω_a. Alkalinity varies by a large range compared to the summer interval, from 1700 to 2100 μeq/kg; however, the variability is more strongly coupled to salinity variability than to any diel pattern. pH_t varies between ~7.9-8.1, and, while late-day maxima correspond to late-day pCO_2 minima, there are additional variations that hint at a relation to salinity. Ω_a varies between ~1-1.5, with an apparent mixture of covariance between salinity and pCO_2.

3.1.5 Single year basic observations

Annual patterns for the representative year 2017 are shown in Figure 6. The leading inferred drivers at the seasonal timescale are the upwelling/downwelling forcing and the related precipitation. In winter, winds are predominantly poleward and lead to onshore convergence and downwelling. Frequently accompanying poleward wind forcing are storm events that bring instances of high precipitation to the bay. In summer, the winds reverse to become primarily equatorward, causing coastal divergence and upwelling. Little precipitation occurs throughout these summer months. Not shown for the location is the

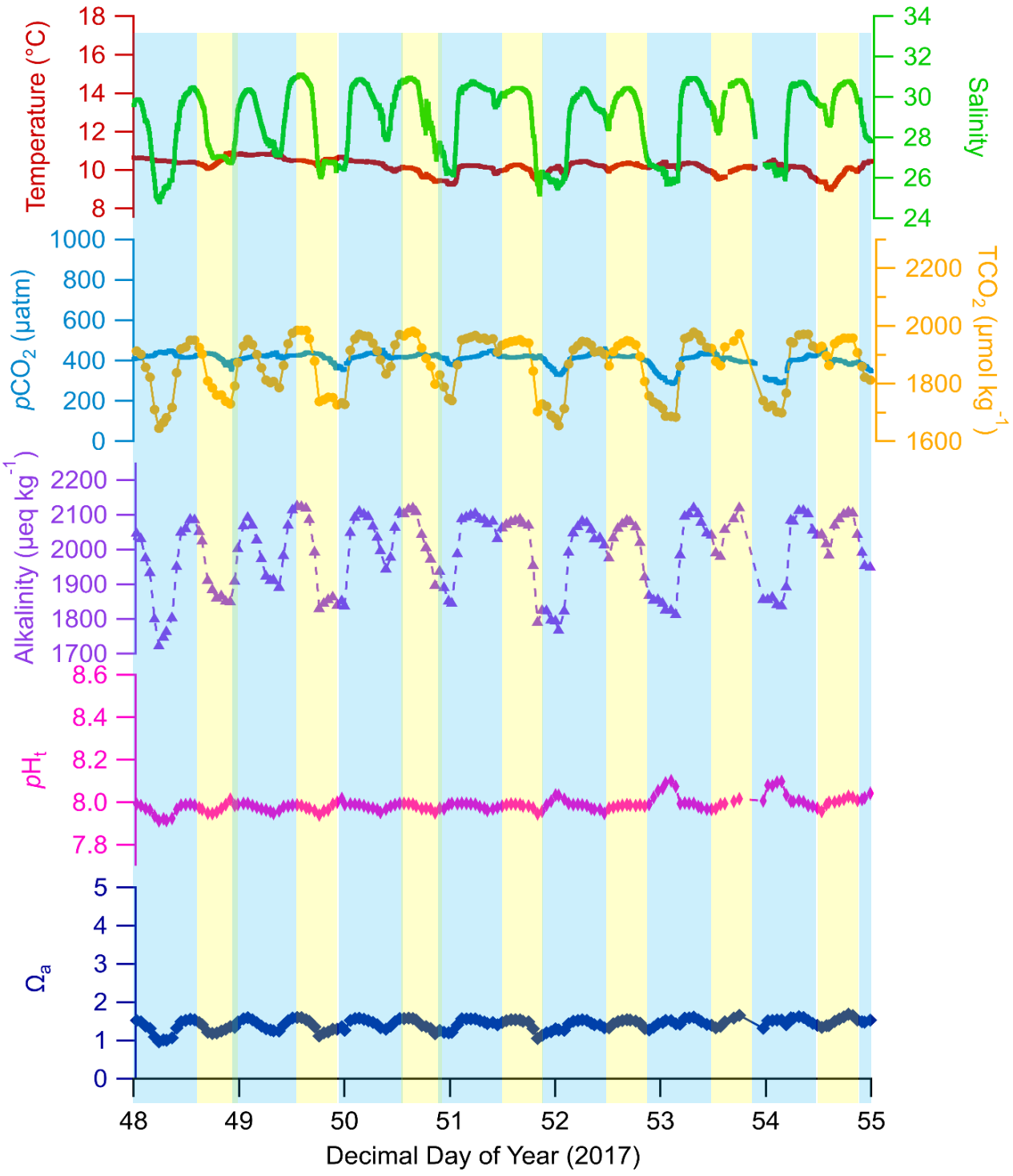

Figure 5. 7-day period winter 2017 for Netarts Bay. pCO_2 (blue line), TCO_2 (orange dots connected by dashed line), and calculated alkalinity (purple triangles connected by dashed line), pH_t (pink diamonds connected by dashed line), and saturation state of aragonite (Ω, blue squares connected by dashed line) for 7 days during a summer period, 2017, at Netarts Bay, OR. Blue shading indicates local nighttime and yellow shading indicates daytime.

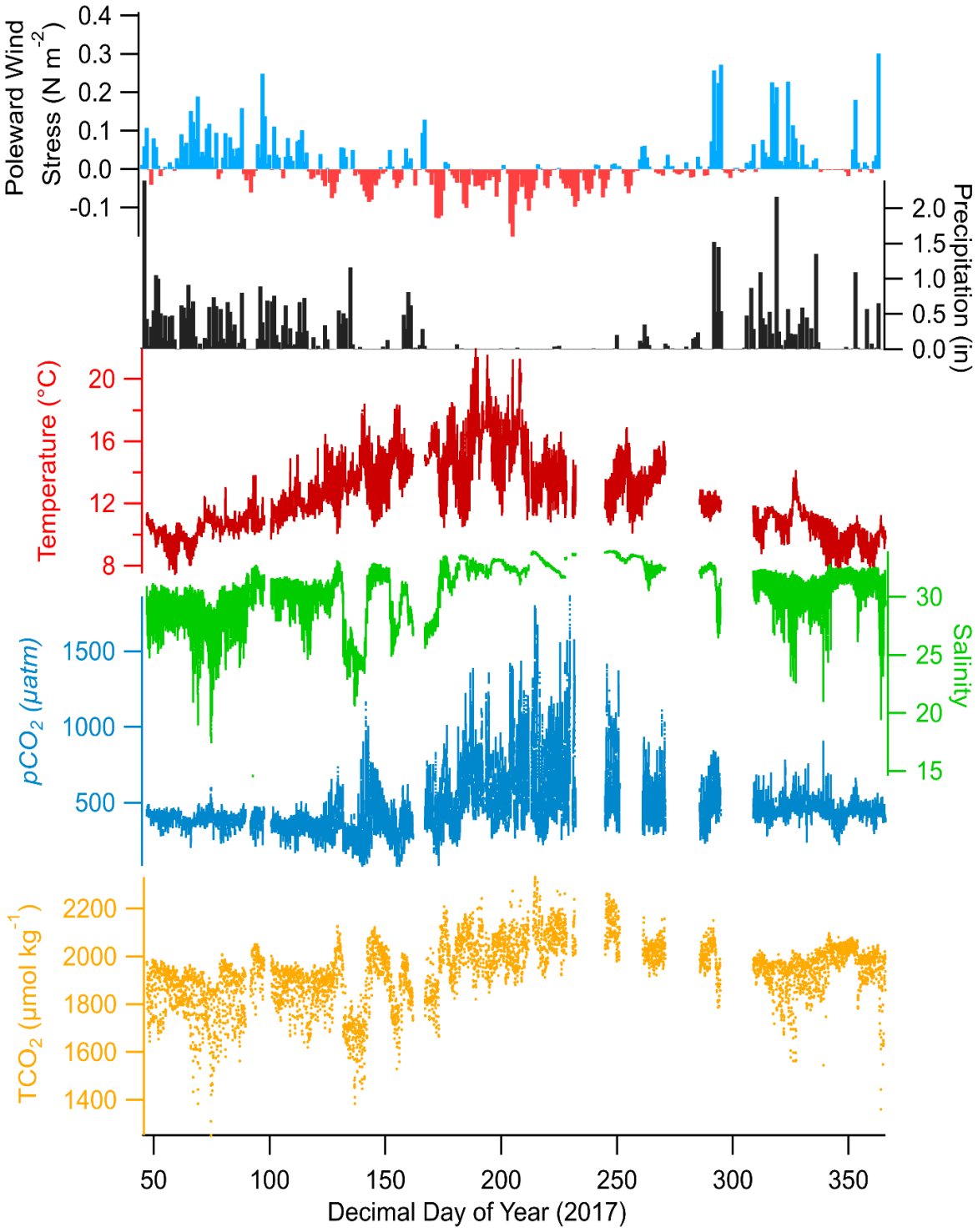

Figure 6. Full 2017-year basic observations for Netarts Bay. Poleward wind stress, daily precipitation, salinity (green line), temperature (red line), pCO_2 (blue line), and TCO_2 (orange dots) for the full 2017 timeseries. Wind stress data courtesy of *http://damp.coas.oregonstate.edu/windstress/;* Precipitation data courtesy of *https://www.ncdc.noaa.gov/cdo-web/*.

annual photoperiod variation from ~8.5 – 15.5 hours between winter and summer solstices. Separating the winter and summer seasons are spring and fall transition periods, where the character of the dominant season fades and that of the impending season grows.

The influence of these seasonal forcings are evident in the temperature and salinity time series. While the coldest temperatures are seen in winter, summertime minimum temperatures are nearly as low (~8 °C), corresponding to the highest bay salinities and reflecting the influence of deep upwelling-source water. However, winter-time temperatures show relatively little variability (8-12°C), with maxima rarely >12 °C, while summer maximum temperatures are frequently > 17 °C. Salinity shows nearly opposite character. The highest values approach 34 in summer, when there is relatively little variability. In contrast, winter salinity is rarely above 32, and minimum values corresponding to high-precipitation events fall as low as 16.

TCO_2 variability show distinctly different behavior from pCO_2 when examined in the composite year as compared to the weekly snapshots. In winter, when pCO_2 variability is minimal, TCO_2 dynamic range is greatest. Winter TCO_2 maxima are only ~2050 µmol/kg, and the lowest annual values, ~1400 µmol/kg are seen then. These low TCO_2 events correspond with freshening events that dilute ocean-source water TCO_2, while having little on pCO_2. During summer, the TCO_2 values are overall higher and show less dynamic range than winter (~2000 – 2250 µmol/kg).

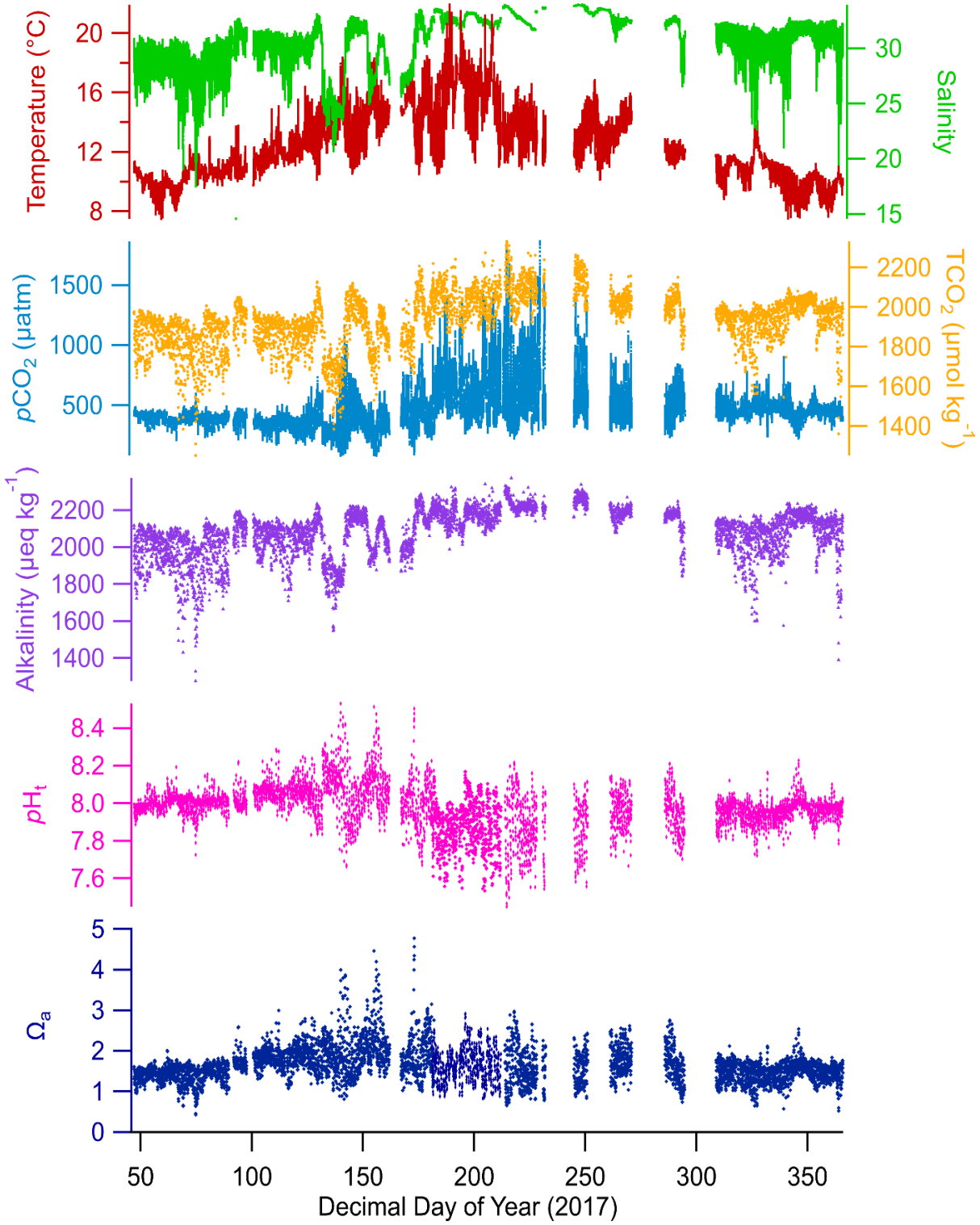

Figure 7. Full 2017-year derived observations for Netarts Bay. pCO_2 (blue line), TCO_2 (orange dots), and calculated alkalinity (purple dots), pH (pink dots), and saturation state of aragonite (Ω, dark blue dots) for the full 2017 timeseries.

3.1.6 Single year derived observations

The full 2017-year observations the derived terms alkalinity, pH_t, and Ω_a are appended to pCO_2, TCO_2, salinity, and temperature time series in Figure 7. Alkalinity shows similar wintertime variability to TCO_2, with lower maximum concentrations (compared to summer) and strong salinity- and TCO_2-covariance leading to a dynamic range of ~1400 - 2200 µmol/kg. During summer, alkalinity reaches its highest values near 2300 µmol/kg, while variability is low with minimum values rarely falling below 2200 µmol/kg. Winter pH_t shows little variability, mostly captured with the range 7.9-8.1, while summer pH_t shows strong variability between 7.5 – 8.4. Wintertime Ω_a generally falls in the range of 1-2, except for some values ~0.5 corresponding to the lowest observed salinities. Summertime dynamic show extreme ranges from ~0.7-5, coinciding with the similarly maximal dynamic range in pCO_2 and pH_t.

3.1.7 Composite year basic observations

Compositing all years' wind stress, precipitation, salinity, temperature, TCO_2, and pCO_2 data provides the full range of variability in the basic carbonate measurements taken at Netarts Bay from 2014 – 2019 (Figure 8). Over all 6 years, temperature ranges from ~5-20 °C, salinity from ~15-34, pCO_2 from ~100-2500 µatm, and TCO_2 from ~1400 -2250 µmol/kg. The 2017-year discussed previously falls within the 6-year composite, and the general patterns hold: winter is dominated by poleward winds and high precipitation, while summer is dominated by equatorward winds and nearly absent precipitation. Wintertime

pCO_2 and temperature exhibit lower variability while summer values show dynamic ranges that nearly encompass the full data-set dynamic range. Wintertime salinity and TCO_2 show lower maxima than seen in summer, and the lowest minima seen all year, while values are higher and less variant in summer. Interannual variability is evident but largely linked to the timing of the seasonal transition and not clearly secular; it is not discussed further here.

3.1.8 Composite-year derived observations

Figure 9 adds all years' calculated alkalinity, pH_t, and Ω_a observations to the previously discussed pCO_2 and TCO_2. Alkalinity ranges from ~1150 - 2400 μeq/kg, pH_t from ~7.5 - 8.6, and Ω_a from ~0.3-5.0. As above, the general patterns seen for the 2017-year persist: Alkalinity is overall lower in winter but experiences the largest variability with extreme minima that correspond to the lowest S events, while summer alkalinity experiences its highest values and lower variability. pH_t variability is low in winter months and exceeds 1 pH unit in summer, coincident with the large observed range in pCO_2. Ω_a shows low variability mostly captured in the range 1-2 in winter, with instances of very low Ω associated with the lowest-S events, while summer conditions show large variability, ranging from 0.7-4.5.

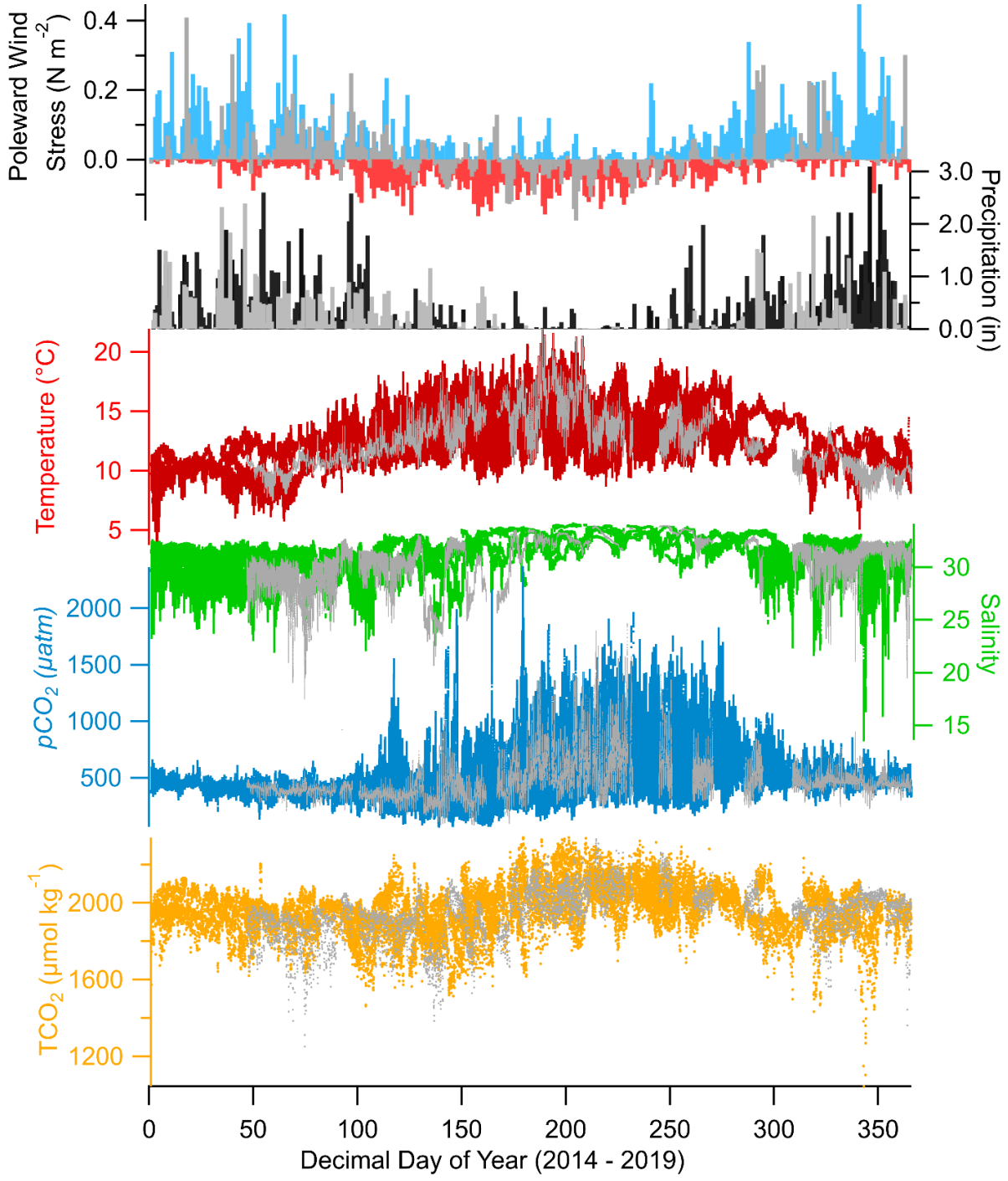

Figure 8. Composite basic observations for Netarts Bay 2014-2019. Poleward wind stress, daily precipitation, salinity (green line), temperature (red line), pCO_2 (blue line), and TCO_2 (orange dots) for all years of 2014-2019. Dark grey shading of each parameter represents the 2017 data set. Wind stress data available at: http://damp.coas.oregonstate.edu/windstress/ Precipitation data courtesy of *https://www.ncdc.noaa.gov/cdo-web/*

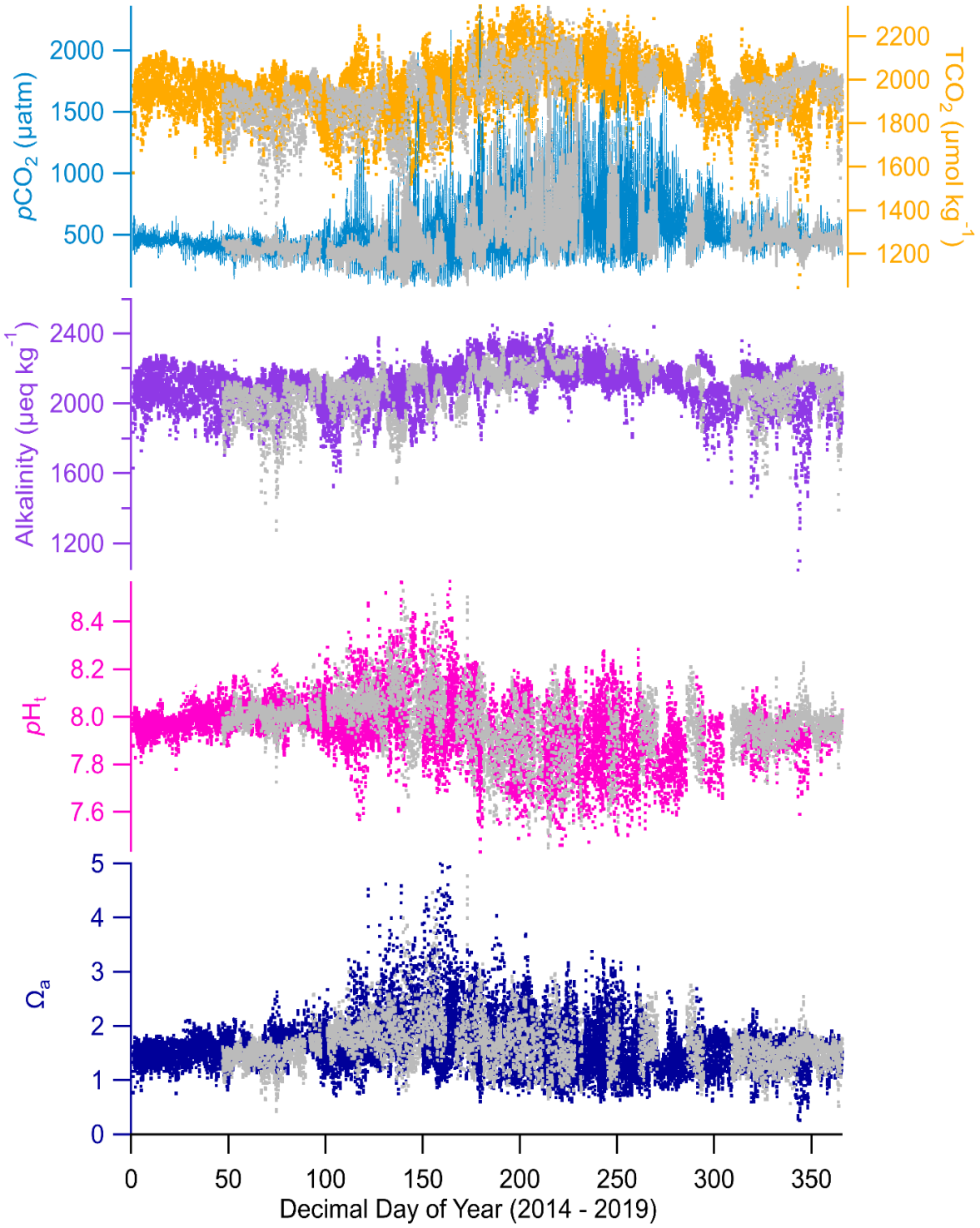

Figure 9. Composite derived observations for Netarts Bay 2014-2019pCO2 (blue line), TCO2 (orange dots), and calculated alkalinity (purple dots), pH (pink dots), saturation state of aragonite (Ω, dark blue dots) for all years of 2014-2019. Time is in decimal day of year (UTC). Dark grey shading of each parameter represents the 2017 data set shown earlier.

4.1 Discussion

4.1.1 Timescales and Drivers of Variability

Netarts Bay experiences dynamic variability across multiple hydrographic and carbonate parameters at timescales from diel to tidal to several days to seasonal. This variability occurs in response to a variety of factors namely in-bay metabolic processes, advection of various water masses into the bay, adjacent coastal wind forcing, and daytime insolation. In this section we examine and hypothesize certain factors driving the observed variability at multiple timescales.

4.1.1.1 Diel Synchrony and Tide Phasing

The previously described diel variability of in-bay pCO_2 is characterized by a gradual decline throughout the afternoon until a diel minimum is reached in late afternoon or early evening, followed by a gradual build up overnight until an early morning maximum is reached. This pattern is evident in both summer and winter, though with lower amplitude in winter (Fig. 2, 3). Coincident with the diel variability, however, is a strong tidal forcing that cannot be clearly separated from the diel forcing in the 1-week snapshots presented earlier. With relatively short water residence times (~12 hours), tidal forcing is evident in salinity, and to some degree TCO_2 and alkalinity variability, particularly in winter. The semi-diurnal tides are not perfectly in phase with the diel variability, however, but shift forward nearly 40 minutes each day. Therefore, if tidal forcing were the dominant

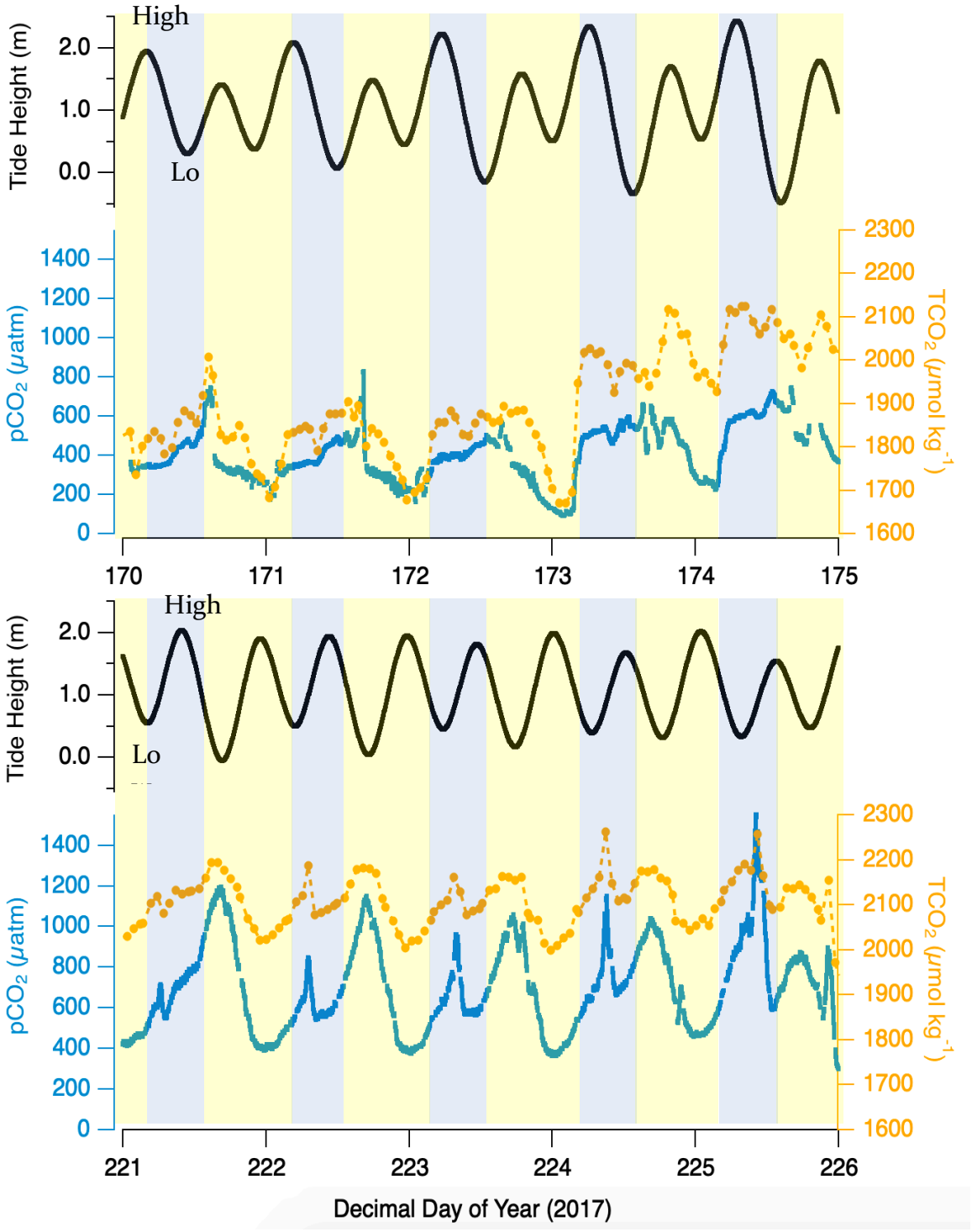

Figure 10. pCO2 (blue line), TCO2 (orange dots connected by a line), and estimated tide height (black line) for two 7-day periods during summer of 2017 with tide-phasing ~90° between top and bottom.

control, we would see the pCO_2 variability reverse phase with respect to the day on ~fortnightly intervals. Figure 10 shows pCO_2 variability across two 5-day periods in summer 2017 with tide phasing shifted roughly 90 degrees between the top and bottom graph. In each representation, pCO_2 trends down during daylight hours to reach a late-day minimum and increases overnight to an early-morning maximum. Similarly, wintertime conditions show diel pCO_2 behavior which trend down in response to daytime insolation and rise slightly overnight (Figure 11) even when comparing periods of orthogonal tide heights.

The apparent driver of this diel variability is the net metabolism driven by a composite of processes in the bay. The balance between primary production, which consumes CO_2 in the presence of sunlight and nutrients to create organic matter, and respiration, which releases CO_2 during the degradation of organic matter, drives diel pCO_2 variability. During summer, when the photoperiod is extended due to higher incident solar angle and prolonged daylight, insolation is at its maxima; coincidentally, upwelling supplies the bay and coastal ocean with elevated nutrients (Oregon coast upwelled-water NO_3^{2-} > 35 μM; Hales et al., 2005). The abundant epibenthic primary producers and the high surface-area:volume ratio of the bay leads to extensive modification of the overlying water, despite rapid tidal flushing. Broadly, the reverse occurs once the lights turn off and heterotrophic metabolism tips the scales, producing an abundance of TCO_2. This addition of dissolved carbon dioxide shifts the carbonate chemistry such that pCO_2 at times passes 2000 μatm as seen in the early morning spring months of 2019.

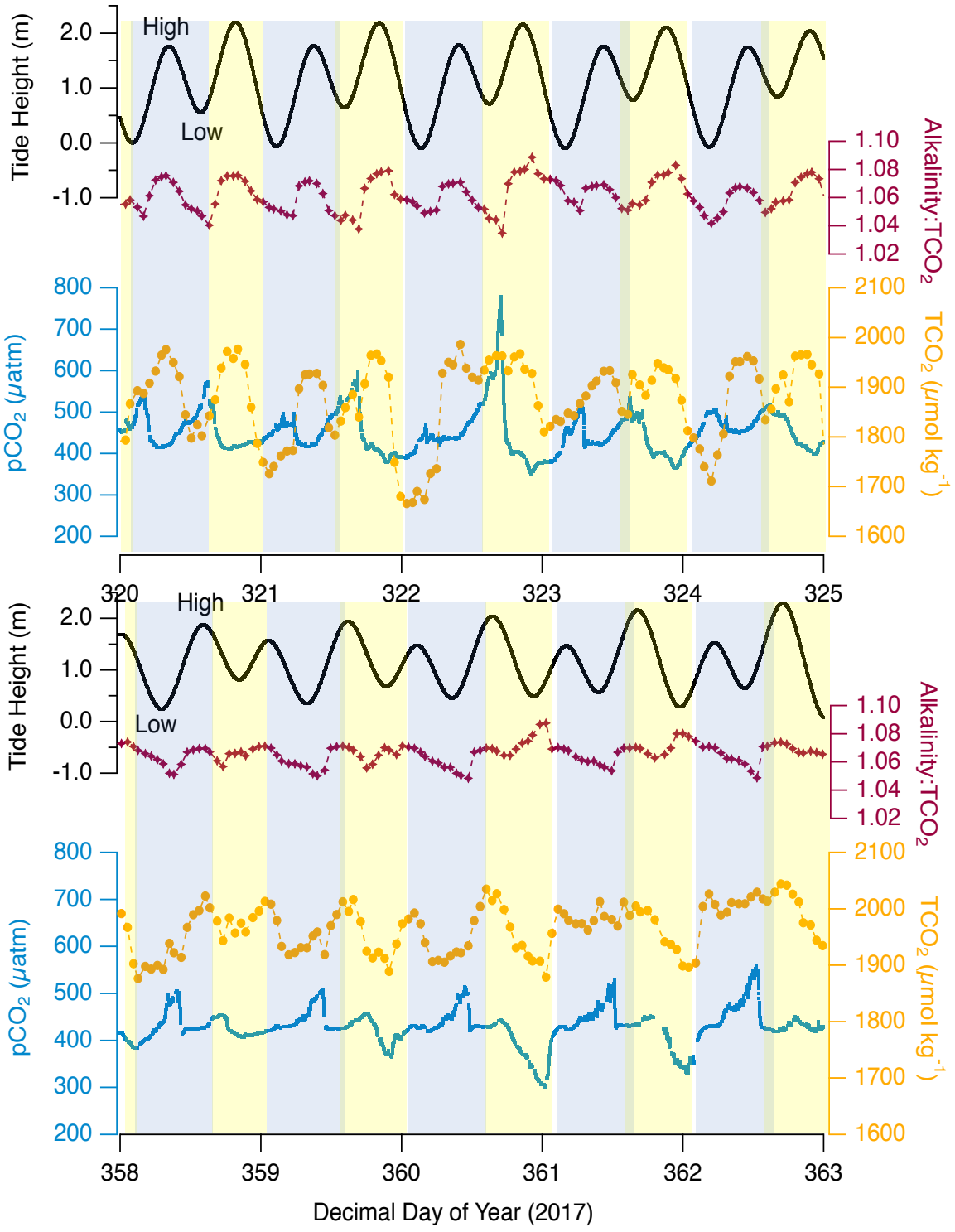

Figure 11. pCO_2 (blue line), TCO_2 (orange dots connected by a line), Alk:TCO_2 ratio (red starts connected by a line), and estimated tide height (black line) for two 5-day periods during winter of 2017 with tide-phasing ~90° between top and bottom; pCO_2 axes have been expanded to emphasize diel features.

This mechanism is supported further by the close coherence of pCO_2 and TCO_2 during the productive summer season, while alkalinity variability remains small. Aerobic net community metabolism impacts primarily TCO_2, with much smaller impact on alkalinity, and thus carries an implied pCO_2 and TCO_2 covariance. For T ~ 12 °C, S ~ 33, the relative change in pCO_2 is 12 times the relative change of TCO_2 (Revelle Factor of 12), for all other variables constant. Peak-peak/minimum relative variability in pCO_2 for the intervals shown ranges from 10-20 times that for TCO_2, adding support to the idea that net metabolism, modulated by diel insolation cycles, is the primary driver of summertime bay carbonate-system variability.

Nested within the day-night variability is an apparent tidal signature, most evident in the "dual-peaks" signature in the pCO_2 behavior in figure 10 (bottom panel). High tides at night deliver relatively lower pCO_2 coastal ocean water into the bay. Rapid tidal flushing and accumulating CO_2 from organisms respiring results in the proceeding low tide to be characterized by elevated pCO_2 and TCO_2

The wintertime conditions are somewhat more challenging to explain, as the diel variability in pCO_2 is muted but persists in the face of clearly tidally-modulated alkalinity and TCO_2. Within broad ranges of TCO_2 and alkalinity, however, pCO_2 is largely driven by changes in the ratio of TCO_2:alkalinity. Although there are important variations in the salinity-alkalinity relationships, discussed below, the leading factor is freshwater dilution of ocean water, which largely preserves the oceanic TCO_2:alkalinity ratio. The large tidally-driven salinity-covariant TCO_2 variability is thus compensated by covarying alkalinity. The

responding factors like pCO_2 and pH show distinct patterns of variability, with the diel character persisting. The metabolic signature is expected to be suppressed relative to summer. Lower insolation angle, shorter photoperiod, and increased cloudiness limit the potential maximum photosynthetic rate, and wintertime coastal waters carry significantly lower nutrient concentrations than upwelled source waters. This reduced metabolic signature is consistent with observed reductions in biomass during winter, when the extensive seagrass coverage seen in summer have vanished.

4.1.1.2 Event-scale Variability

Imposed onto the observed carbonate dynamics are event-scale processes which act on timescales of several days to weeks. The predominantly summertime equatorward winds which drive offshore Ekman transport and upwelling occur in cycles of strong wind-forcing/relaxation periods. The duration, timing of onset, and intensity of these cycles are governed by synoptic-scale high-pressure systems and occur on variable time and space scales along the West Coast (Aristizábal et al., 2017; Pringle & Dever, 2009). One such transition from wind relaxation to upwelling is captured in Figures 2, 4, which show a clear hydrographic and carbonate-variable influence of high salinity, high TCO2 and alkalinity deep-upwelled-source water entering the bay coincident with a strengthening of equatorward wind. The wind-relaxation event which occurred prior, days 169-173, was concurrent with lowered salinity, TCO2 and alkalinity below 2000 μmol/kg and 2100 μm/kg, respectively. The wind-stress time-series for the full year 2017 (Figure 6) shows

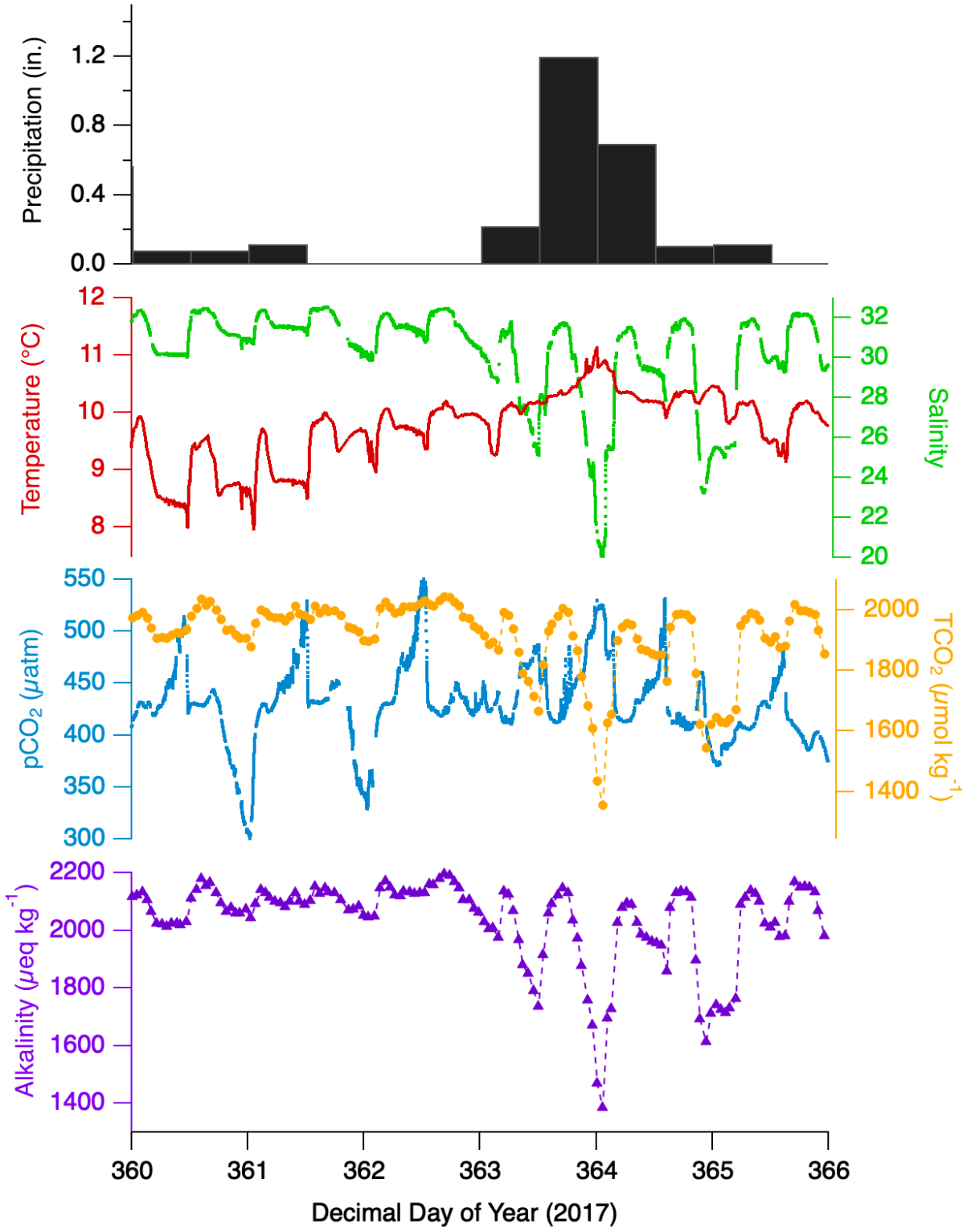

Figure 12. Winter precipitation event variability across a 5-day interval during December of 2017 for all hydrographic and carbonate variable parameters. Precipitation data for Netarts Bay courtesy of www.ncdc.noaa.gov

intervals of intensified summertime equatorward wind occurring on timescales of several days to weeks followed by instances of brief relaxation periods and/or poleward winds. These relaxation cycles coincide with warmer water temperatures, lower and more tidally synchronized salinity and alkalinity, and a slight dampening of diel pCO_2 dynamics in response to less input of dissolved nutrients as the bay's primary water source shifts from deep upwelled water to open Pacific Ocean surface water.

Event-scale variability occurs throughout the downwelling-wintertime regime as well as when the influence of predominantly low-salinity California current water is interrupted by brief but intense storm-dominated conditions. Figure 12 represents one instance during the winter of 2017, when multiple cold-fronts moved over the Oregon coast depositing several inches of rain over a 48-hour window (days 363-365). The combination of direct dilution and mixing of local coastal freshwater endmembers represented by discharge from small mountainous rivers results in large negative salinity, alkalinity, and TCO_2 departures from the overall background downwelling conditions. Rapid tidal flushing and a return to precipitation-free downwelling in the days following storm conditions quickly returns the bay to normal wintertime variability.

4.1.1.2 Seasonal Upwelling and Downwelling

At seasonal timescales, we observe large differences in character and variability of nearly all hydrographic and carbonate parameters between the summer and winter. The clear driver of these stark summer-winter differences is the regional transition from

upwelling-dominated high-insolation summer conditions with equatorward winds and low precipitation, to downwelling-dominated low-insolation winter conditions with frequent intense precipitation events. These background seasonal differences set the stage for the distinct behavior and variability timescales seen in the different seasons.

Interceding these two states are transition seasons where the character of the dominant season fades and the impending season emerges. In the fall transition, upwelling favorable winds wane in the September-October timeframe, while the winter storms build in October-November. In the spring transition, intervals between winter storm events have building upwelling character. The bay's seasons are thus driven largely by the initiation and termination of coastal upwelling and downwelling. There have been detailed studies regarding the variability of the onset of upwelling in this region (Pierce et al., 2006); similarly wintertime precipitation events are highly variable interannually.

4.1.2. Behavior of Alkalinity

For much of the open surface ocean, alkalinity is affected primarily by local removal (by evaporation and/or ice formation) and addition (by precipitation and/or ice-melt) of near zero-alkalinity fresh water (Brewer et al., 1986; Lee et al., 2006). Mixing of water masses results in single, conservative (linear) alkalinity-salinity relationships that can be applied within large oceanic sub-regions (Takahashi et al., 2014). We have compared regionally published alkalinity-salinity relationships for North Pacific subregion (Cullison Gray et al., 2011; Takahashi et al., 2014) to that acquired from the WCSH measurements

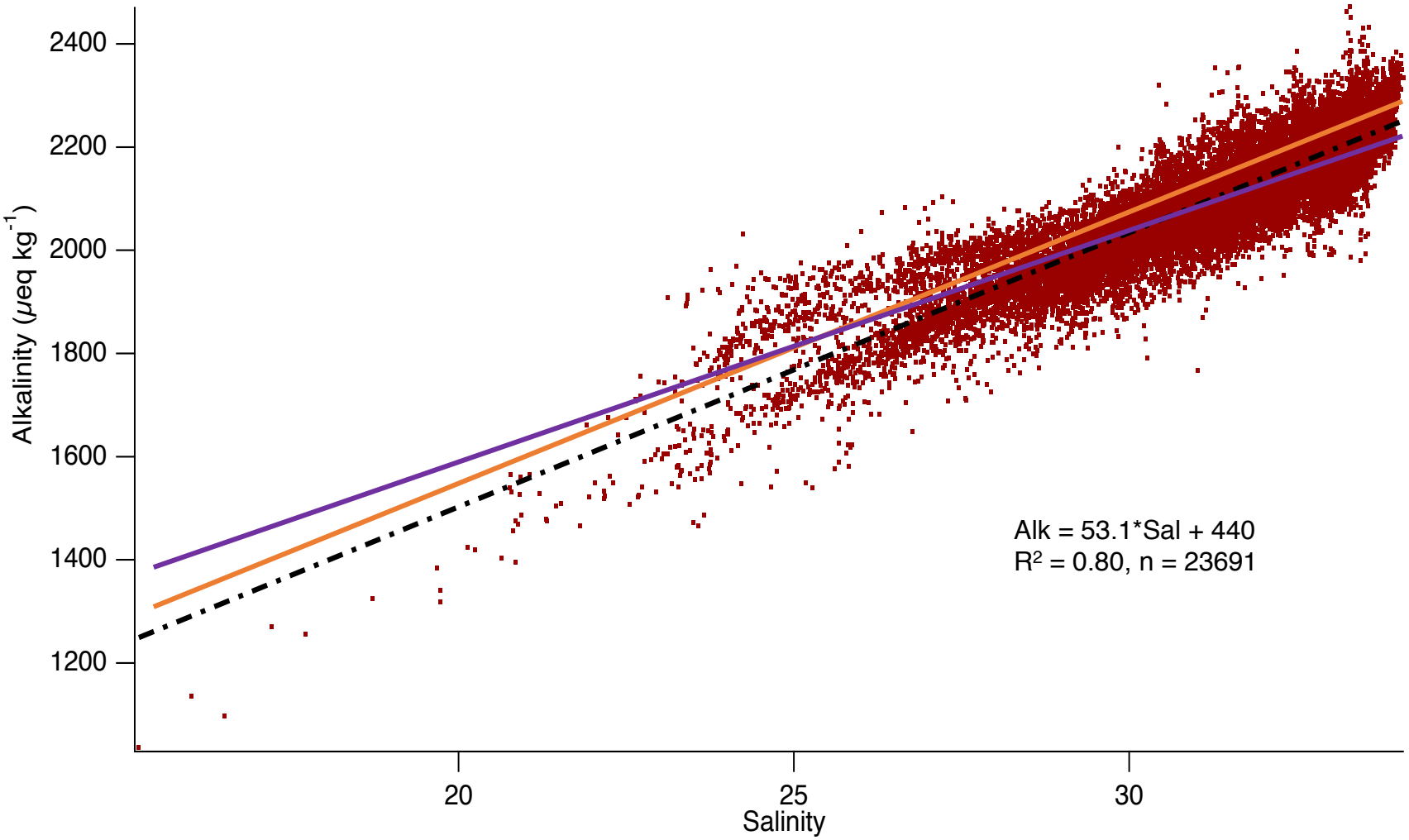

Figure 13. Composite alkalinity-salinity plot for all years 2014 – 2019. Red dots represent hourly data and black dashed line represents a simple linear-fit to our data. Alkalinity-salinity regressions are overlain using published regional values from C. Grey et al. (2011; orange), and Takahashi et al. (2014; purple).

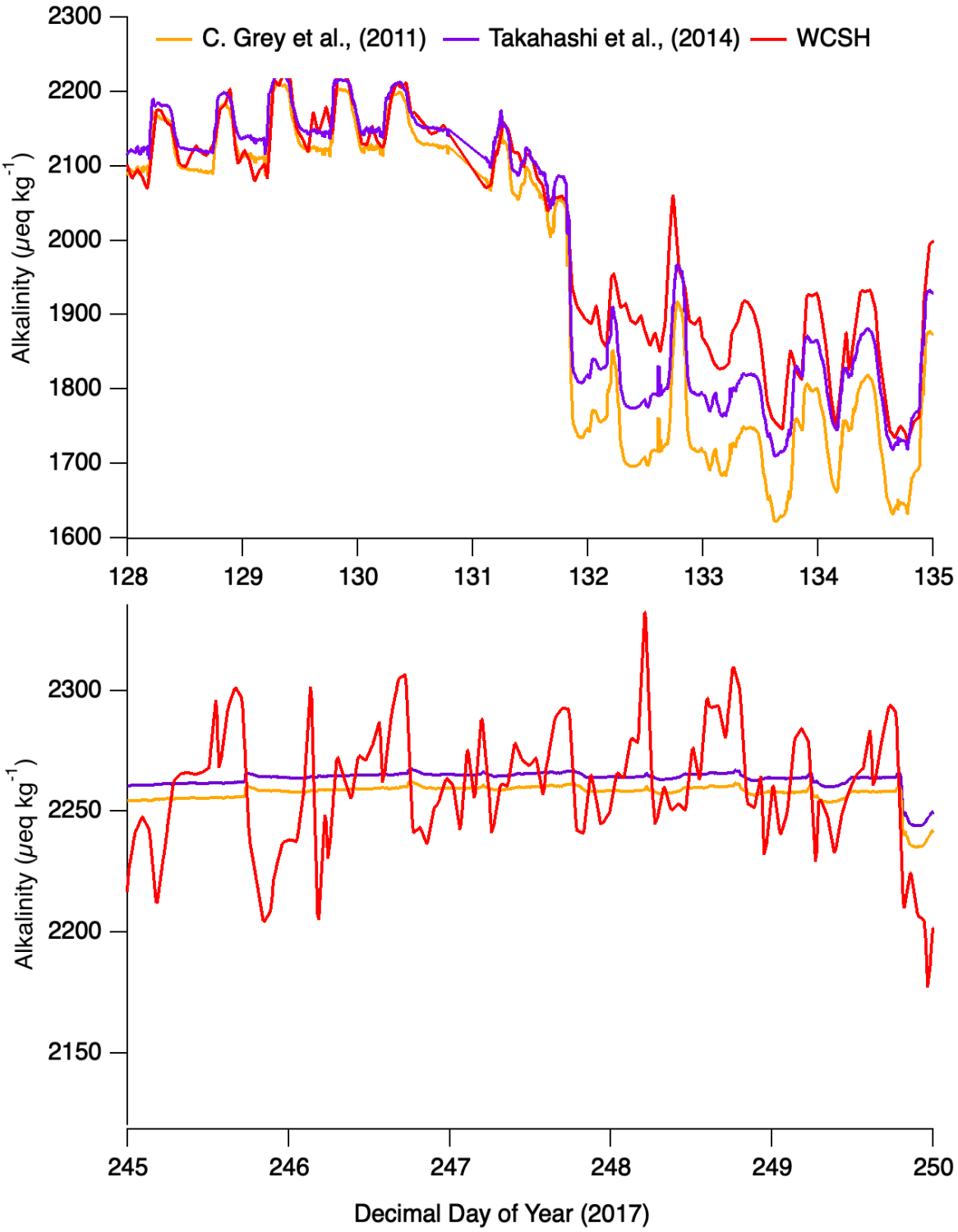

Figure 14. Reconstruction and comparison of WCSH alkalinity against three published regional alkalinity-salinity relationships for both winter downwelling (top) and summertime upwelling conditions (bottom).

(Figure 13), and while these measurements are broadly consistent with the community, specifically at salinities approaching open Pacific Ocean surface waters (>32), there are multiple and discrete trends which depart from both the regional relationships and one composite WCSH alkalinity/salinity relationship.

The alkalinity-salinity relationships established by Takahashi et al. (2014) and Grey et al., (2011) for the North Pacific surface ocean, combined with measured salinity and pCO_2 at WCSH allows prediction of in-bay alkalinity. The result is relatively strong predictive capability, especially during downwelling conditions (average deviations ~15 μeq/kg) but poor predictive capability during the upwelling season when salinities remain high and alkalinity behaves non-conservatively (Figure 14). The apparent difference in predictive capabilities is likely due to sub-oxic metabolic processes that create or remove alkalinity, and the influence of coastal freshwater endmembers that are not captured by open Pacific Ocean surface waters—discussed in more detail below. Variability in the predictive capabilities of regional alkalinity-salinity relationships is evident in Figure 14 (top panel), which shows coherence among all three models during intervals of strong alkalinity-salinity coupling, such as precipitation-free downwelling favorable conditions. These models tend to underestimate bay alkalinity at lower salinities during day of year 132-135 when the Columbia River plume appears to advect southward and into the bay (discussed below). The apparent metabolic influence on alkalinity during summertime upwelling results in additional failure in the predictive capabilities of regional alkalinity models. We believe the presence of multiple freshwater endmembers and the existence of sub-oxic metabolic processes limit how we can apply the model. Further, significant departures in

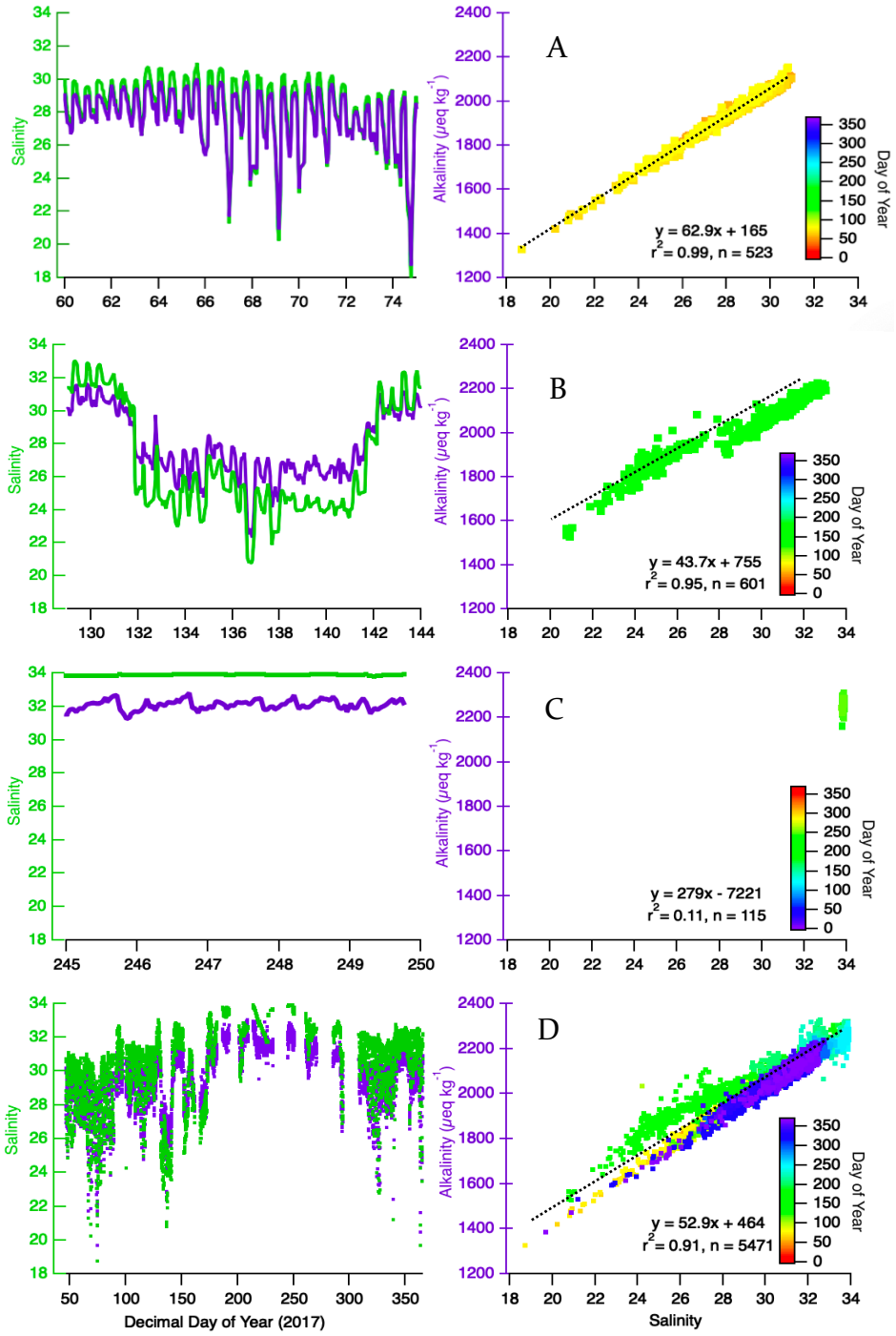

Figure 15. Alkalinity-salinity time-series of three discrete alkalinity-salinity relationships and their associated regression statistics at WCSH for the year 2017; color bar represents day of year. A: wintertime downwelling and mixing of local freshwater with Pacific open ocean water; B: southward advection of the Columbia River plume from days 132-142; C: summertime upwelling and evidence of non-conservative alkalinity-salinity behavior; and D: the full year 2017 alkalinity-salinity time series.

calculated WCSH carbonate variables, pH_t and Ω_a, and those predicted by regional relationships necessitates identification of multiple-end members and hypotheses of potential drivers in the observed departure of alkalinity-salinity behavior.

4.1.2.1 Identifying Multiple End-Members

During the winter and spring-transition months, salinity variability is high and metabolic activity in the bay is suppressed, as discussed previously. Alkalinity-salinity regressions over a variety of timescales are highly linear with R^2 values frequently exceeding 0.9 (Figure 15A). However, there is clear evidence that there are multiple alkalinity-salinity relationships (Figure 15D). In winter, when metabolic effects are minimized and local precipitation is high, these regressions typically carry higher alkalinity-salinity slopes (<55 μmol/kg per S), and low apparent freshwater end-members (<500 μmol/kg), compared to regional estimates of alkalinity-salinity dependence. In the transition between the summer and winter seasons, precipitation events decrease, while salinity and covariant alkalinity variability remains high. Under these conditions, alkalinity-salinity regressions are also highly linear, but show lower slopes (<50 μmol/kg per S) and higher freshwater endmembers (> 800 μmol/kg) than published regional relationships. These high-correlation, high salinity-variability conditions can be delineated into two groups, each with a common northern California Current surface seawater endmember with distinct freshwater endmembers. In the first case, the freshwater endmember is some combination of truly alkalinity-free precipitation that falls directly on the bay, the low-alkalinity streams that drain into it, and the accumulation of low-alkalinity small-mountainous river

freshwater (Hales et al., 2016; Wetz et al., 2006; Whitney & Garvine, 2006) in inner shelf waters over the winter season. In the second, the Columbia River plume is the suspected freshwater endmember. During persistent downwelling conditions, the Columbia River plume is transported northward close to the Washington coast, while during upwelling conditions, the plume is transported over 100 km south of Netarts Bay, but is typically displaced offshore to the shelf break (Banas et al., 2009). During the spring transition, upwelling conditions can establish the plume's presence southward, but disruption of upwelling by strong downwelling events will push the southward extension of the plume onshore before it is completely deflected to the north (Mazzini et al., 2015). One such event occurred during May of 2017 (Figure 15B), clearly identifiable by an alkalinity-salinity mixing curve significantly elevated above the background wintertime mixing curve.

4.1.2.2 Metabolic-process Dominance

The strong alkalinity-salinity coupling observed during downwelling-favorable conditions tends to break down during persistent upwelling intervals (Figure 15C). During these summertime conditions, precipitation and local-river discharge is absent, the Columbia River plume is far offshore, and the in-bay salinity variability is minimal. In spite of this, alkalinity variability is high and significantly in excess of our analytical uncertainty. Even when regressions were statistically significant with high linearity, the coefficients were geochemically unrealistic: slopes with magnitudes many times any reported values and with both positive and negative sign. These results suggested that any alkalinity-

salinity covariance was fortuitous, and that the alkalinity variability was driven by processes other than mixing or dilution/concentration.

Non-physical processes that can change bay alkalinity include the consumption/release of protons in proportion to nitrate uptake/regeneration during oxic photosynthesis/respiration; $CaCO_3$ formation and dissolution; and suboxic respiration such as sulfate reduction and pyrite formation. While any of these processes are probably occurring, net calcification seems most likely to have the greatest effect. Aerobic nitrate cycling should result in anti-correlated alkalinity:TCO_2 with a ~1:7 ratio, and this is not evident. Further, net autotrophy within the bay, as suggested by the seasonal buildup of seagrass beds, would seemingly result in a growing alkalinity over the course of the summer season, which is also not observed. In contrast, summer alkalinity departs negatively from expected salinity dependences. The only process that can drive these negative departures in the face of strong biological pCO_2 depletion is net precipitation of $CaCO_3$. It is hard to quantify the net $CaCO_3$ precipitation independently, but the bay is a location of abundant and resilient shellfish communities.

4.1.2.3 Hybrid Alkalinity Model

We desired to resolve variable carbonate parameters between hourly TCO_2 measurements because there is evidence of dynamics occurring at sub-hourly scales, such as pCO_2 spikes routinely measured during the late-evening/mid-morning hours of spring/summer that were only intermittently captured by the hourly TCO_2 analyses (Figure

2). Our initial goal was to develop an alkalinity model which would allow us to in-fill calculated carbonate parameters at the resolution of the pCO_2 data product. However, while there is an overall salinity dependence on alkalinity (Figure 13, 15), there exist multiple discrete salinity dependencies that one single relationship does not fully capture, discussed above. During winter, alkalinity-salinity has covariance resulting in robust and meaningful linear regression statistics, and, as previously stated, summertime alkalinity-salinity regressions produce slopes and intercepts at times hundreds of times larger than winter with no mechanistic relevance or predictive capability. Analysis of several published

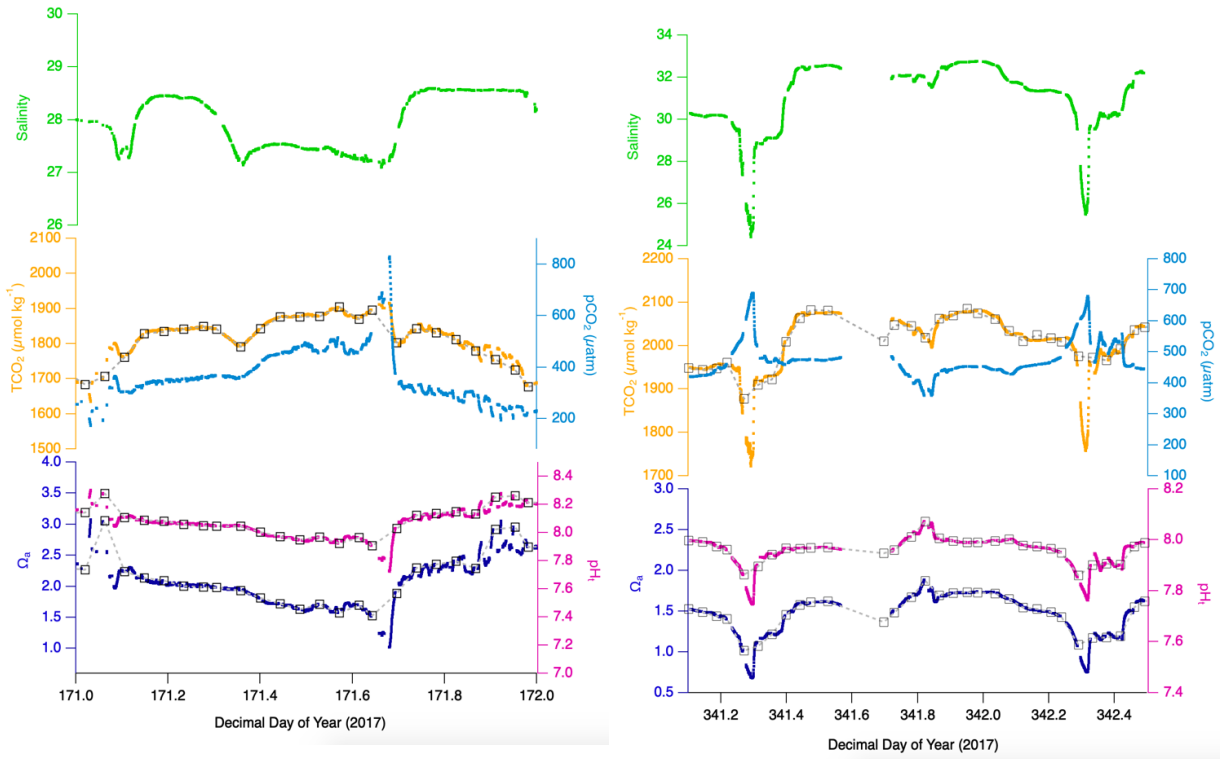

Figure 16. Carbonate parameters, TCO_2, pH, and Ω_a resolved at the resolution of the pCO_2 and salinity data. Symbols represent hourly calculated carbonate variables, while infilling represents data calculated using the running piecewise regression algorithm. On the left, a summer period using pure time-interpolated alkalinity-salinity, and right, a winter interval using a running piecewise linear regression.

regional alkalinity-salinity relationships at times results in poor predictability of in-bay carbonate dynamics (Cullison Gray et al., 2011; Lee et al., 2006; Takahashi et al., 2014), especially during upwelling events (Figure 15).

The solution was a hybrid alkalinity model consisting of a forward moving, piecewise linear regression for winter months of November through March, and a simple time-interpolated alkalinity product for the months of April-October. The piecewise linear regression utilizes a linear least squares bisector calculation to account for measurement uncertainties in both salinity and alkalinity, while retaining regressions with meaningful regression coefficients and rejecting those with negative or overtly large slopes and/or intercepts (see Appendix I).

Figure 16 demonstrates application of the hybrid alkalinity model for summer (left) and winter (left). For winter, the piecewise linear regression model is applied to an interval during December 2017 and the associated regression statistics are provided in Table 2. While pCO_2 variability is minimal for this day compared to summer, small-scale, sub-hourly structure has been successfully resolved for TCO_2, *p*H, and Ω_a as evidenced by negative TCO_2 deviations of nearly ~150 μmol/kg between instances of hourly measurements coinciding with sub-hourly negative salinity departures. Similarly, high-resolution calculations of *p*H and Ω_a reveal sub-hourly behavior that would otherwise not be captured using hourly measurements. The development of this algorithm thus allows the user to in-fill variable carbonate parameters at the resolution of pCO_2 using measured

salinity. Additionally, gaps in data coverage of either pCO_2 or TCO_2 can now be estimated using output from the regression models and pairing it with temperature and salinity data.

4.1.3 Implications for Ocean Acidification

WCSH experienced the immediate impacts of ocean acidification during the 2008 growing season when intake water containing naturally elevated CO_2 –further enhanced by anthropogenic CO_2—killed off millions of larval shellfish, placing the hatchery in danger of permanent shutdown (Barton et al., 2012, 2015). Along the adjacent coastal shelf, water influenced by anthropogenic carbon has been documented upwelling onto the shelf (Feely et al., 2008), creating potentially corrosive conditions for marine calcifiers and threatening to fundamentally alter the marine food-web. Instances of ocean acidification-related shellfish mortality and various other implications of changing carbonate chemistry are expected to continue worsening through the end of century (IPCC, 2018), and the work of coastal monitoring and public communication and engagement will prove essential towards developing potential mitigation strategies.

4.1.3.1 Ocean Acidification Detection

In the coastal environment with dramatically variable carbonate chemistry within relatively small spatial scales, monitoring ocean acidification requires a broad network of buoys, field scientists, and volunteers. These operations are often times many millions of

dollars (Strong et al., 2014) and the commercial fisheries and shellfish industries rely on accurate, reliable assessment of coastal water quality as it relates to specific organisms. Frequently, *p*H probes are used to measure *p*H because they are relatively easy tools to use. However, *p*H measurements come with inherent measurement uncertainties and often are unreliable predictors of more relevant ocean acidification parameters, such as Ω_a (Giminez et al., 2019). A three-year study of Willapa Bay carbonate chemistry revealed that for a nominal *p*H value of 7.7, Ω_a ranged from <0.5-1.5 (Hales et al., 2017) suggesting that deployment of *p*H probes may fail to detect biologically relevant ocean acidification parameters and may lead to devastating loss for shellfish hatchery operators. For a nominal pH of 7.7 across all years at WCSH, Ω_a ranges from 0.9-1.8.

4.1.3.2 Frequency of Low Omega Conditions

Understanding and predicting organismal response to ocean acidification represents a primary challenge in determining the fate of marine calcifiers in the face of an increasingly corrosive marine environment. It is now well understood that the saturation state—not pH—is the most biologically relevant parameter in determining the success of larval shellfish calcification (Waldbusser et al., 2015). Laboratory studies suggest that exposure to saturation states below 1.7 induces physiological stress among *Crassostrea gigas* (Pacific oyster); below 1.4 significant stunting and potential larval shellfish mortality can occur (Barton et al., 2012; Waldbusser et al., 2015); while Ω_a < 1.0 and the system thermodynamically favors dissolution of mineral calcium carbonate back into solution.

Utilizing hourly calculated Ω_a at WCSH for all years of this study, Ω_a measured less than 1.7 occurred during 58% of instances, <1.4 for 31% of instances, and <1.0 6% of the time, with the most frequent events <1.4 occur during the late-summer months (Fig 9, bottom). While the ecological thresholds for optimal and suboptimal shellfish spawning are well known for Pacific oysters, the exact timing of larval shellfish spawning remains an ongoing research question. For WCSH, few native oyster populations are found within the bay owing in part to lack of suitable substrate, while mussels are found inhabiting the rocky tidal shores near the mouth of the bay. Clams represent the dominant native shellfish population of Netarts Bay. The success of any native shellfish population which may inhabit the bay is critically dependent on overlapping spawning times with optimal carbonate conditions—particularly within the first 48-hours when shellfish are at the highest risk of mortality in corrosive conditions (Waldbusser et al., 2015).

4.1.3.3 Anthropogenic CO_2

The global ocean inventory of CO_2 is increasing at a rate of approximately 0.41±0.13 mol C/m^2/yr (0.82±0.26 Pg C/yr) (Quay et al., 2017) primarily by means of ocean surface gas exchange with the atmosphere. Various estimates place the total increase in concentration of oceanic TCO_2 due to anthropogenic input on the order of 30-60 μmol/kg depending on latitude and depth (Khatiwala et al., 2013). Using a nominal value 35 μmol/kg ($\Delta TCO_{2,anth}$) added to the oceans since 1850, we can coarsely estimate what conditions would have been like for WCSH without any added anthropogenic carbon.

On average, the addition of 35 µmol/kg TCO_2 to the oceans has resulted in average WCSH *p*H and Ω_a values approximately 0.1 and 0.30 units lower, respectively, when compared to pre-industrial estimates. This is in line with global evaluations that surface ocean *p*H has declined 0.1 units since the start of the Industrial Revolution (Feely et al., 2004) and that surface ocean saturation state is in a current state of global decline (Friedrich et al., 2012; Jiang et al., 2015). Applying a conservative fixed anthropogenic TCO_2 addition of 35 µmol/kg for all years 2014-2019 (Figure 17), we find the relative impact of

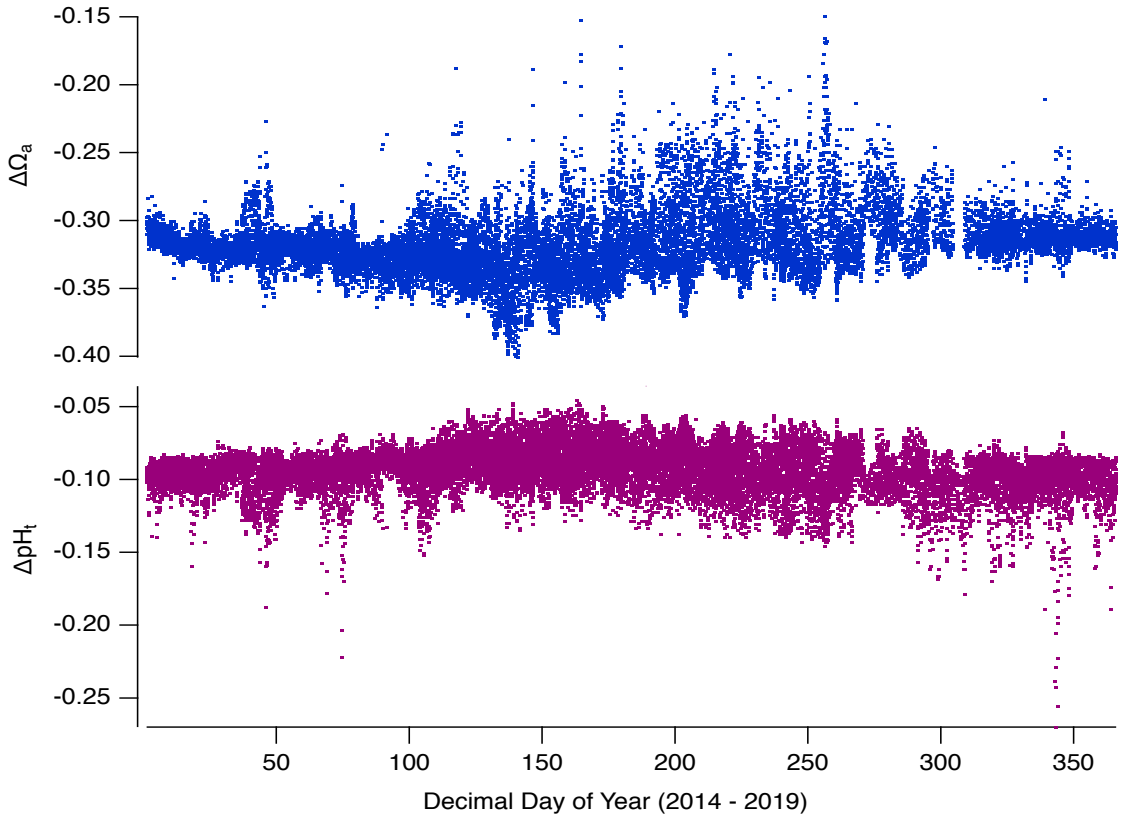

Figure 17. ΔpH and $\Delta\Omega_a$ calculated for all years 2014-2019 at WCSH using a nominal anthropogenic TCO_2 concentration of 35 µmol/kg. Values represent approximate negative departures in observed pH and Ω_a as a result of anthropogenic CO_2 since 1850.

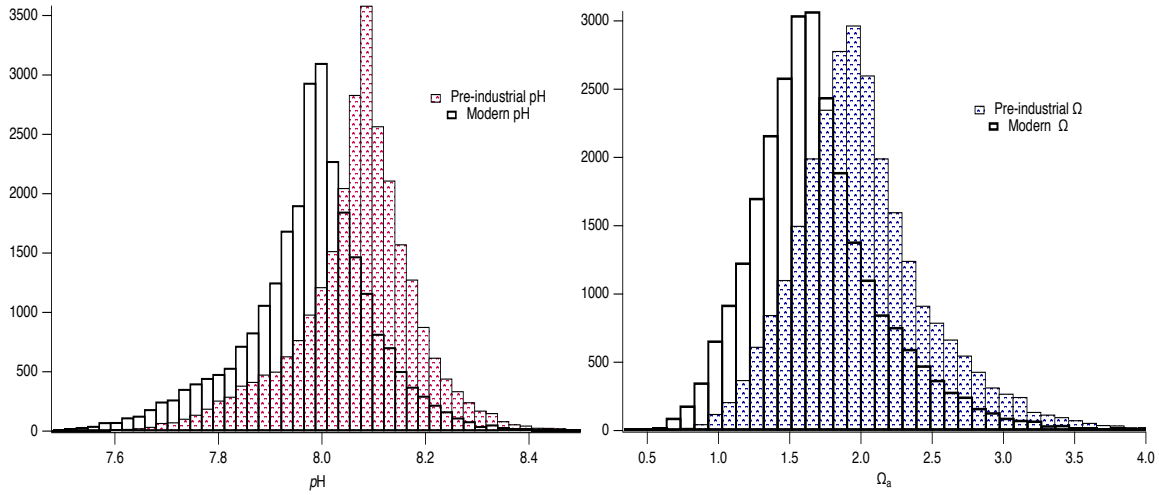

Figure 18. Histogram representations of pre-industrial and modern calculations of pH (left) and saturation state (right) for 6-years at WCSH, 2014-2019.

anthropogenic carbon on *p*H and Ω_a is variable throughout upwelling and downwelling events and across multiple years (Table 1). Astoundingly, when Ω_a conditions are at their best during the late-spring/early-summer months (Figure 9, bottom panel), the apparent contribution of anthropogenic carbon is at its greatest. Moreover, the contribution of $\Delta TCO_{2,anth}$ to *p*H appears to be at its annual minima during this period, suggesting there is a decoupling mechanism between *p*H and the more biologically relevant Ω_a parameter. Implementing a fixed anthropogenic carbon reveals both a decline in the mean pH and saturation state, as well as more frequent low-pH, low-saturation state events (Figure 18). Continued oceanic uptake of carbon will continue to push *p*H and Ω_a below their modern values, with high-latitude surface waters expected to be fully undersaturated by the end of century (Feely et al., 2009).

Table 1. Average and standard deviations for calculated ΔpH and $\Delta\Omega_a$ using a nominal anthropogenic TCO_2 value of 35 µmol/kg for all years, binned by season.

	Season	Winter	Spring Transition	Summer	Fall Transition
ΔpH $\Delta\Omega_a$	2014	-0.11 ± 0.01 -0.32 ± 0.01	-0.09 ± 0.01 -0.33 ± 0.02	-0.10 ± 0.02 -0.30 ± 0.04	-0.11 ± 0.02 -0.31 ± 0.02
	2015	-0.10 ± -0.02 -0.31 ± 0.01	-0.09 ± 0.01 -0.33 ± 0.02	-0.09 ± 0.02 -0.31 ± 0.03	-0.10 ± 0.01 -0.30 ± 0.02
	2016	-0.10 ± 0.01 -0.32 ± 0.01	-0.08 ± 0.01 -0.33 ± 0.02	-0.08 ± 0.01 -0.32 ± 0.03	-0.10 ± 0.1 -0.28 ± 0.03
	2017	-0.10 ± 0.01 -0.32 ± 0.01	-0.09 ± 0.01 -0.34 ± 0.02	-0.09 ± 0.03 0.31 ± 0.03	-0.09 ± 0.01 -0.32 ± 0.01
	2018	-0.09 ± 0.01 -0.32 ± 0.01	-0.09 ± 0.01 -0.33 ± 0.02	-0.09 ± 0.01 -0.31 ± 0.03	-0.09 ± 0.01 -0.31 ± 0.02
	2019	-0.09 ± 0.01 0.32 ± 0.01	-0.09 ± 0.01 -0.32 ± 0.02	-0.09 ± 0.01 -0.31 ± 0.03	n/a n/a

Future Work

The data record presented here is unique in terms of duration, resolution, and carbonate-system constraint. It captures magnitudes and scales of variability previously unknown. Despite the 6-year length of record, and clear differences among years, identification of a secular trend in any parameter is challenging in the face of the background natural variability and such analysis is beyond the scope of this study. A tantalizing observational result lies in the variation between years in the onset and duration of the transition seasons. While the composite-year time-series show consistent behavior within the characteristically-defined summer and winter seasons, there is less consistency in the initiations and terminations of these seasons, and in the nature of the transitions between them. Continued monitoring of Netarts Bay will be useful in understanding how ocean acidification will continue to impact the sensitive coastal ecosystems and expand our understanding of high-resolution carbonate chemistry within estuaries.

Conclusion

Netarts Bay is a metabolically dynamic, oceanic-dominated estuarine environment with hydrographic and carbonate variability occurring on multiple timescales. Summer upwelling, wintertime downwelling, and in-situ bay biogeochemistry represent significant drivers of the observed variability in carbonate dynamics. Applying a conservative estimate of how much anthropogenic carbon has been added to the surface ocean reveals that

Netarts Bay has seen a decline in pH and saturation state of 0.1 units and 0.35, respectively, since the early 1800's. The bay's waters routinely become undersaturated during the late evenings and early mornings of the productive summer season. Sub-hourly resolution of pH and saturation state provide additional insight into what is governing observed carbonate dynamics and how frequently low-omega events are occurring.

Chapter 3 – Conclusions

High-resolution carbonate measurements of pCO_2 and hourly TCO_2 provided at WCSH in Netarts Bay represent the ongoing monitoring efforts to sample coastal ocean carbonate chemistry and observe and establish trends, specifically in the context of ocean acidification. While the length of this 6-year time-series is too limited to develop or hypothesize about interannual trends, it is apparent that Netarts Bay has been impacted broadly by the additional input of anthropogenic carbon.

Netarts Bay is a marine-dominated, macrotidal estuary exhibiting variable carbonate chemistry from time-scales of sub-hourly, to diel, to weekly, to seasonally. Variability on the diel is represented by the balance between autotrophic and heterotrophic organisms, the intensity and duration of daytime insolation, and the relative concentration of dissolved nutrients in the water column. Primary production during daytime consumes CO_2 until a daily minimum is reached in late-afternoon or early evening, with pCO_2 at times measured <200 μatm. Net heterotrophy at nighttime results in late-evening/early-morning pCO_2 diel maxima, with values at times surpassing >2300 μatm, especially during the early summer months. These diel patterns are observed throughout all months of the year and across all 6-years represented in this study.

Event-scale variability in summertime and wintertime is driven primarily by offshore wind conditions and the rapid tidal-flushing which can restore in-bay hydrographic and carbonate parameters to average conditions in less than 24 hours following strong precipitation events. On seasonal timescales, the presence of large-scale high- and low-pressure systems drive offshore wintertime downwelling and summertime

upwelling, and contribute to both the overall metabolic state of the bay and the observed hydrographic variability. Wintertime downwelling conditions are coincident with muted pCO_2 dynamics, with alkalinity and TCO_2 dynamics largely covariant with tidally driven changes in salinity, while water temperatures are on average cooler. Delivery of high concentrations of dissolved nutrients paired with extended photoperiods during summertime upwelling result in large diel pCO_2 dynamics, and elevated salinity (>33.5) paired with delivery of high-alkalinity, high-TCO_2 waters into the bay. A host of processes which produce or consume alkalinity, such as $CaCO_3$ formation/dissolution, and/or oxic and sub-oxic metabolism result in alkalinity-salinity relationships that become non-conservative during these summer months. Intervening upwelling and downwelling are brief transition periods during which time offshore wind conditions change poleward, diel hydrographic variability becomes more tidally covariant, and the net metabolic state of the bay is reduced.

Analysis of alkalinity-salinity relationships, both derived from WCSH measurements and those calculated from published regional relationships reveal variable fresh-water endmembers entering the bay throughout the year. Mixing of small mountainous rivers, southward advection of the Columbia River plume, open surface Pacific Ocean water, California Current water, deep-upwelled Pacific Ocean water, and direct precipitation represent the many distinct water masses that enter the bay during the year. Robust alkalinity-salinity relationships during the winter season allow us to implement a running piecewise linear regression, the output of which we can use to infill carbonate variables at the resolution of the pCO_2 data. This algorithm allows infilling of

*p*H, Ω_a, and TCO_2 in-between hourly TCO_2 measurements and resolves sub-hourly structure to these variables that may go uncaptured by the hourly TCO_2 measurements. However, implementation of this moving piecewise regression during the productive summer months results in slopes and intercepts with no real mechanistic or predictive value. Instead, we use a pure time-interpolation for the months of April-October, and rely on the piecewise regression for November-March. The hybrid alkalinity-salinity model results in the full suite of carbonate parameters calculated at the high-resolution pCO_2 data product.

The broader context of this study is the increasing acidity of our oceans and the addition of 0.82±0.26 Pg C/yr due to anthropogenic causes. Conservative estimates place the global ocean inventory of anthropogenic carbon to have added ~35 μmol/kg TCO_2 since the Industrial Revolution. For Netarts Bay, the net addition of ~35 μmol/kg TCO_2 has resulted in a decline of ~0.1 *p*H units, and ~0.32 Ω_a. There is no apparent year-to-year variability in these values, but there is clear annual variability. The impact of anthropogenic carbon on Ω_a appears to be most magnified during the late-spring/early-summer months, during which time calculated Ω_a is actually the most favorable for organisms. This suggests that the favorable Ω_a conditions already observed in the months of April-June would be even *more* favorable in the absence of anthropogenic carbon.

Continued monitoring at WCSH is necessary to establish longer term trends in saturation state and *p*H, among other variables. Additionally, networks of high-resolution carbonate measurements are strongly suggested in order to model how ocean acidification and further alterations will impact the highly variable domains of coastal ecosystems.

Citations

Aristizábal, M. F., Fewings, M. R., & Washburn, L. (2017). Effects of the Relaxation of Upwelling-Favorable Winds on the Diurnal and Semidiurnal Water Temperature Fluctuations in the Santa Barbara Channel, California. *Journal of Geophysical Research: Oceans*, *122*(10), 7958–7977. https://doi.org/10.1002/2017JC013199

Banas, N. S., MacCready, P., & Hickey, B. M. (2009). The Columbia River plume as cross-shelf exporter and along-coast barrier. *Continental Shelf Research*, *29*(1), 292–301. https://doi.org/10.1016/j.csr.2008.03.011

Bandstra, L., Hales, B., & Takahashi, T. (2006). High-frequency measurements of total CO2: Method development and first oceanographic observations. *Marine Chemistry*, *100*(1), 24–38. https://doi.org/10.1016/j.marchem.2005.10.009

Barton, A., Hales, B., Waldbusser, G. G., Langdon, C., & Feely, R. A. (2012). The Pacific oyster, Crassostrea gigas, shows negative correlation to naturally elevated carbon dioxide levels: Implications for near-term ocean acidification effects. *Limnology and Oceanography*, *57*(3), 698–710. https://doi.org/10.4319/lo.2012.57.3.0698

Barton, A., Waldbusser, G., Feely, R., Weisberg, S., Newton, J., Hales, B., et al. (2015). Impacts of Coastal Acidification on the Pacific Northwest Shellfish Industry and Adaptation Strategies Implemented in Response. *Oceanography*, *25*, 146–159. https://doi.org/10.5670/oceanog.2015.38

Brewer, P. G., Bradshaw, A. L., & Williams, R. T. (1986). Measurements of Total Carbon Dioxide and Alkalinity in the North Atlantic Ocean in 1981. In J. R. Trabalka & D. E. Reichle (Eds.), *The Changing Carbon Cycle: A Global Analysis* (pp. 348–370). New York, NY: Springer. https://doi.org/10.1007/978-1-4757-1915-4_18

Cullison Gray, S. E., DeGrandpre, M. D., Moore, T. S., Martz, T. R., Friederich, G. E., & Johnson, K. S. (2011). Applications of in situ pH measurements for inorganic carbon calculations. *Marine Chemistry*, *125*(1), 82–90. https://doi.org/10.1016/j.marchem.2011.02.005

Diaz, R. J., & Rosenberg, R. (1995). Marine benthic hypoxia: a review of its ecological effects and the behavioural responses of benthic macrofauna. *Oceanography and Marine Biology: An Annual Review*. Retrieved from http://www.emodnet-biology.eu/data-catalog?module=ref&refid=234458&printversion=1&dropIMIStitle=1

Diaz, Robert J. (2001). Overview of Hypoxia around the World. *Journal of Environmental Quality*, *30*(2), 275–281. https://doi.org/10.2134/jeq2001.302275x

Diaz, Robert J., & Rosenberg, R. (2008a). Spreading Dead Zones and Consequences for Marine Ecosystems. *Science*, *321*(5891), 926–929. https://doi.org/10.1126/science.1156401

Diaz, Robert J., & Rosenberg, R. (2008b). Spreading dead zones and consequences for marine ecosystems. *Science (New York, N.Y.)*, *321*(5891), 926–929. https://doi.org/10.1126/science.1156401

England, A. H., Duffin, A. M., Schwartz, C. P., Uejio, J. S., Prendergast, D., & Saykally, R. J. (2011). On the hydration and hydrolysis of carbon dioxide. *Chemical Physics Letters*, *514*(4), 187–195. https://doi.org/10.1016/j.cplett.2011.08.063

Evans, W., Hales, B., & Strutton, P. G. (2011). Seasonal cycle of surface ocean pCO_2 on the Oregon shelf. *Journal of Geophysical Research. Oceans; Washington*, *116*(5). http://dx.doi.org.ezproxy.proxy.library.oregonstate.edu/10.1029/2010JC006625

Evans, W., Hales, B., & Strutton, P. G. (2013). pCO_2 distributions and air–water CO_2 fluxes in the Columbia River estuary. *Estuarine, Coastal and Shelf Science*, *117*, 260–272. https://doi.org/10.1016/j.ecss.2012.12.003

Evans, W., Pocock, K., Hare, A., Weekes, C., Hales, B., Jackson, J., et al. (2019). Marine CO_2 Patterns in the Northern Salish Sea. *Frontiers in Marine Science*, *5*. https://doi.org/10.3389/fmars.2018.00536

Feely, R. A., Sabine, C. L., Lee, K., Berelson, W., Kleypas, J., Fabry, V. J., & Millero, F. J. (2004). Impact of Anthropogenic CO_2 on the $CaCO_3$ System in the Oceans. *Science*, *305*(5682), 362–366. https://doi.org/10.1126/science.1097329

Feely, R. A., Sabine, C. L., Hernandez-Ayon, J. M., Ianson, D., & Hales, B. (2008). Evidence for Upwelling of Corrosive "Acidified" Water onto the Continental Shelf. *Science*, *320*(5882), 1490–1492. https://doi.org/10.1126/science.1155676

Feely, R. A., Doney, S. C., & Cooley, S. R. (2009). Ocean acidification : present conditions and future changes in a high-CO2 world. https://doi.org/10.5670/oceanog.2009.95

Foster, G. L., Royer, D. L., & Lunt, D. J. (2017). Future climate forcing potentially without precedent in the last 420 million years. *Nature Communications*, *8*, 14845. https://doi.org/10.1038/ncomms14845

Friedrich, T., Timmermann, A., Abe-Ouchi, A., Bates, N. R., Chikamoto, M. O., Church, M. J., et al. (2012). Detecting regional anthropogenic trends in ocean acidification against natural variability. *Nature Climate Change*, *2*(3), 167–171. https://doi.org/10.1038/nclimate1372

Gattuso, J.-P., & Hansson, L. (2011). *Ocean Acidification*. OUP Oxford.

van Geen, A., Takesue, R. K., Goddard, J., Takahashi, T., Barth, J. A., & Smith, R. L. (2000). Carbon and nutrient dynamics during coastal upwelling off Cape Blanco, Oregon. *Deep Sea Research Part II: Topical Studies in Oceanography*, *47*(5), 975–1002. https://doi.org/10.1016/S0967-0645(99)00133-2

Glanzman. (1971). *Tidal Hydraulics, Flushing Characteristics and Water Quality of Netarts Bay*. Oregon State University, Dept. of Civil Engineering.

Gruber, N., Clement, D., Carter, B. R., Feely, R. A., Heuven, S. van, Hoppema, M., et al. (2019). The oceanic sink for anthropogenic CO2 from 1994 to 2007. *Science*, *363*(6432), 1193–1199. https://doi.org/10.1126/science.aau5153

Hales, B., Chipman, D., & Takahashi, T. (2004). High-frequency measurement of partial pressure and total concentration of carbon dioxide in seawater using microporous hydrophobic membrane contactors. *Limnology and Oceanography: Methods*, *2*(11), 356–364. https://doi.org/10.4319/lom.2004.2.356

Hales, B., Suhrbier, A., Waldbusser, G. G., Feely, R. A., & Newton, J. A. (2017). The Carbonate Chemistry of the "Fattening Line," Willapa Bay, 2011-2014. *Estuaries and*

Coasts; Port Republic, *40*(1), 173–186. http://dx.doi.org.ezproxy.proxy.library.oregonstate.edu/10.1007/s12237-016-0136-7

Hales, B., Takahashi, T., & Bandstra, L. (2005). Atmospheric CO_2 uptake by a coastal upwelling system. *Global Biogeochemical Cycles*, *19*(1). https://doi.org/10.1029/2004GB002295

Howland, R. J. ., Tappin, A. ., Uncles, R. ., Plummer, D. ., & Bloomer, N. . (2000). *Distributions and seasonal variability of pH and alkalinity in the Tweed Estuary, UK. Science of The Total Environment, 251-252, 125–138.* doi:10.1016/s0048-9697(00)00406-x

Ianson, D., Allen, S. E., Harris, S. L., Orians, K. J., Varela, D. E., & Wong, C. S. (2003). The inorganic carbon system in the coastal upwelling region west of Vancouver Island, Canada. *Deep Sea Research Part I: Oceanographic Research Papers*, *50*(8), 1023–1042. https://doi.org/10.1016/S0967-0637(03)00114-6

Intergovernmental Panel on Climate Change (Ed.). (2014). *Climate Change 2013 - The Physical Science Basis: Working Group I Contribution to the Fifth Assessment Report of the Intergovernmental Panel on Climate Change*. Cambridge: Cambridge University Press. https://doi.org/10.1017/CBO9781107415324

Jiang, L.-Q., Feely, R. A., Carter, B. R., Greeley, D. J., Gledhill, D. K., & Arzayus, K. M. (2015). Climatological distribution of aragonite saturation state in the global oceans. *Global Biogeochemical Cycles*, *29*(10), 1656–1673. https://doi.org/10.1002/2015GB005198

Kennish, M. J. (2002). Environmental threats and environmental future of estuaries. *Environmental Conservation*, *29*(1), 78–107. https://doi.org/10.1017/S0376892902000061

Khatiwala, S., Tanhua, T., Mikaloff Fletcher, S., Gerber, M., Doney, S. C., Graven, H. D., et al. (2013). Global ocean storage of anthropogenic carbon. *Biogeosciences*, *10*(4), 2169–2191. https://doi.org/10.5194/bg-10-2169-2013

Lee, K., Tong, L. T., Millero, F. J., Sabine, C. L., Dickson, A. G., Goyet, C., et al. (2006). Global relationships of total alkalinity with salinity and temperature in surface

waters of the world's oceans. *Geophysical Research Letters*, *33*(19). https://doi.org/10.1029/2006GL027207

Mazzini, P., Risien, C., Barth, J. *et al.* Anomalous Near-Surface Low-Salinity Pulses off the Central Oregon Coast. *Sci Rep* **5,** 17145 (2015). https://doi.org/10.1038/srep17145

McCallum, L. (2000). *Netarts Bay, Oregon: an assessment of human impact on an estuarine system*. https://doi.org/10.15760/etd.2548

Mulder, R. (2000). *Regional tectonic deformation of the northern Oregon coast as recorded by Pleistocene marine terraces*. https://doi.org/10.15760/etd.6317

Nemcek, N., Ianson, D., & Tortell, P. D. (2008). A high-resolution survey of DMS, CO2, and O2/Ar distributions in productive coastal waters. *Global Biogeochemical Cycles*, *22*(2). https://doi.org/10.1029/2006GB002879

Peirson, W., Davey, E., Jones, A., Hadwen, W., Bishop, K., Beger, M., et al. (2015). Opportunistic management of estuaries under climate change: A new adaptive decision-making framework and its practical application. *Journal of Environmental Management*, *163*, 214–223. https://doi.org/10.1016/j.jenvman.2015.08.021

Pierce, S. D., Barth, J. A., Thomas, R. E., & Fleischer, G. W. (2006). Anomalously warm July 2005 in the northern California Current: Historical context and the significance of cumulative wind stress. *Geophysical Research Letters*, *33*(22), L22S04. https://doi.org/10.1029/2006GL027149

Pringle, J. M., & Dever, E. P. (2009). Dynamics of wind-driven upwelling and relaxation between Monterey Bay and Point Arena: Local-, regional-, and gyre-scale controls. *Journal of Geophysical Research: Oceans*, *114*(C7). https://doi.org/10.1029/2008JC005016

Quay, P., Sonnerup, R., Munro, D., & Sweeney, C. (2017). Anthropogenic CO2 accumulation and uptake rates in the Pacific Ocean based on changes in the 13C/12C of dissolved inorganic carbon. *Global Biogeochemical Cycles*, *31*(1), 59–80. https://doi.org/10.1002/2016GB005460

Rabalais, N. N., Turner, R. E., Diaz, R. J., & Justic, D. (2009). Global change and eutrophication of coastal waters. *ICES Journal of Marine Science*, *66*(7), 1528–1537. https://doi.org/10.1093/icesjms/fsp047

Rabalais, Nancy N., Turner, R. E., & Wiseman, W. J. (2002). Gulf of Mexico Hypoxia, a.k.a. "The Dead Zone." *Annual Review of Ecology and Systematics*, *33*, 235–263.

Reid, P. C., Fischer, A. C., Lewis-Brown, E., Meredith, M. P., Sparrow, M., Andersson, A. J., et al. (2009). Chapter 1. Impacts of the oceans on climate change. *Advances in Marine Biology*, *56*, 1–150. https://doi.org/10.1016/S0065-2881(09)56001-4

Shirzad. (1988). *Physical and Hydrologic Characteristics, the Oregon Estuaries*. Strategic Assessment Branch, Ocean Assessments Division, Office of Oceanography and Marine Assessment, National Ocean Service, National Oceanic and Atmospheric Administration.

Strong, A. L., Kroeker, K. J., Teneva, L. T., Mease, L. A., & Kelly, R. P. (2014). Ocean Acidification 2.0: Managing our Changing Coastal Ocean Chemistry. *BioScience*, *64*(7), 581–592. https://doi.org/10.1093/biosci/biu072

Takahashi, T., Sutherland, S. C., Chipman, D. W., Goddard, J. G., Ho, C., Newberger, T., et al. (2014). Climatological distributions of pH, pCO2, total CO2, alkalinity, and CaCO3 saturation in the global surface ocean, and temporal changes at selected locations. *Marine Chemistry*, *164*, 95–125. https://doi.org/10.1016/j.marchem.2014.06.004

Talmage, S. C., & Gobler, C. J. (2010). Effects of past, present, and future ocean carbon dioxide concentrations on the growth and survival of larval shellfish. *Proceedings of the National Academy of Sciences of the United States of America*, *107*(40), 17246–17251. https://doi.org/10.1073/pnas.0913804107

Vance, Jesse M. (2012, July 13). *Proof-of-Concept: Automated high-frequency measurements of pCO_2 and TCO_2 and real-time monitoring of the saturation state of calcium carbonate.* (Thesis). Oregon State University. Retrieved from https://ir.library.oregonstate.edu/concern/graduate_projects/br86b7957

Waldbusser, G. G., & Salisbury, J. E. (2014). Ocean Acidification in the Coastal Zone from an Organism's Perspective: Multiple System Parameters, Frequency Domains, and Habitats. *Annual Review of Marine Science*, *6*(1), 221–247. https://doi.org/10.1146/annurev-marine-121211-172238

Waldbusser, G. G., Voigt, E. P., Bergschneider, H., Green, M. A., & Newell, R. I. E. (2011). Biocalcification in the Eastern Oyster (Crassostrea virginica) in Relation to Long-term Trends in Chesapeake Bay pH. *Estuaries and Coasts*, *34*(2), 221–231.

Waldbusser, G. G., Hales, B., Langdon, C. J., Haley, B. A., Schrader, P., Brunner, E. L., Gray, M. W., Miller, C. A., Gimenez, I., et al. (2015). Ocean Acidification Has Multiple Modes of Action on Bivalve Larvae. *PLOS ONE*, *10*(6), e0128376. https://doi.org/10.1371/journal.pone.0128376

Waldbusser, G. G., Hales, B., Langdon, C. J., Haley, B. A., Schrader, P., Brunner, E. L., Gray, M. W., Miller, C. A., & Gimenez, I. (2015). Saturation-state sensitivity of marine bivalve larvae to ocean acidification. *Nature Climate Change*, *5*(3), 273–280. https://doi.org/10.1038/nclimate2479

Wetz, M. S., Hales, B., Chase, Z., Wheeler, P. A., & Whitney, M. M. (2006). Riverine Input of Macronutrients, Iron, and Organic Matter to the Coastal Ocean off Oregon, U.S.A., during the Winter. *Limnology and Oceanography*, *51*(5), 2221–2231.

White, M. M., McCorkle, D. C., Mullineaux, L. S., & Cohen, A. L. (2013). Early exposure of bay scallops (Argopecten irradians) to high CO_2 causes a decrease in larval shell growth. *PLoS ONE*, *8*(4), e61065. https://doi.org/10.1371/journal.pone.0061065

Whiting, M. C., & McIntire, C. D. (1985). An Investigation of Distributional Patterns in the Diatom Flora of Netarts Bay, Oregon, by Correspondence Analysis1. *Journal of Phycology*, *21*(4), 655–661. https://doi.org/10.1111/j.0022-3646.1985.00655.x

Whitney, M. M., & Garvine, R. W. (2006). Simulating the Delaware Bay Buoyant Outflow: Comparison with Observations. *Journal of Physical Oceanography*, *36*(1), 3–21. https://doi.org/10.1175/JPO2805.1

Zeebe, R. E. (2012). History of Seawater Carbonate Chemistry, Atmospheric CO2, and Ocean Acidification. *Annual Review of Earth and Planetary Sciences*, *40*(1), 141–165. https://doi.org/10.1146/annurev-earth-042711-105521

Appendices

Appendix I. Regression output from the hybrid alkalinity-salinity model

Table 2. Piecewise, forward moving alkalinity-salinity regression output from one 24-hour interval in December 2017. Data visualized in Figure 16.

Day of Year	Alkalinity	Salinity	Slope	Intercept	R^2	Slope deviation	Intercept deviation	Average Absolute Deviation
341.098	2111	30.75	68.8	-4	0.9947	3.17	97.6	4.77
341.142	2073	30.03	47.1	658	0.9837	3.81	114.5	9.29
341.185	2046	29.62	45.1	709	0.9751	4.50	133.5	8.49
341.227	2035	29.40	44.3	733	0.9729	4.61	135.6	8.35
341.270	2042	29.52	47.3	647	0.9751	4.72	139.5	10.58
341.312	2061	29.85	50.0	570	0.9848	3.90	116.5	11.34
341.353	2083	30.18	52.7	492	0.9873	3.75	113.4	11.99
341.397	2103	30.53	53.6	467	0.9890	3.55	108.6	13.63
341.458	2128	31.06	60.0	265	0.9964	2.28	70.8	6.71
341.517	2154	31.51	57.0	357	0.9941	2.77	87.5	6.49
341.578	2179	31.94	58.7	305	0.9791	5.37	171.5	6.87
341.639	2187	32.05	57.3	352	0.9675	6.53	209.2	6.99
341.699	2189	32.03	59.8	274	0.9800	5.35	171.3	4.31
341.761	2189	32.05	58.0	330	0.9817	4.96	159.0	4.47
341.822	2191	32.07	60.0	265	0.9806	5.28	169.5	5.26
341.863	2206	32.35	65.4	91	0.9492	9.32	301.6	6.12
341.907	2212	32.43	54.2	454	0.9557	7.22	234.0	3.96
341.950	2209	32.39	54.7	437	0.9680	6.20	200.7	4.04
341.992	2203	32.35	72.4	-140	0.9670	8.32	269.2	7.17
342.035	2195	32.20	63.2	160	0.9627	7.72	248.7	8.00
342.077	2184	32.03	63.4	154	0.9678	7.20	230.7	7.91
342.118	2168	31.82	62.2	190	0.9663	7.22	229.7	7.31
342.162	2144	31.27	43.6	780	0.9669	5.02	157.0	10.99
342.205	2122	30.88	43.8	770	0.9614	5.44	168.1	11.40
342.247	2105	30.64	44.7	735	0.9354	7.20	220.7	12.79
342.290	2097	30.45	46.5	682	0.9257	8.02	244.4	12.53
342.332	2099	30.55	43.6	766	0.9521	6.05	184.8	10.15
342.373	2105	30.67	45.1	723	0.9627	5.51	169.1	10.25
342.417	2115	30.82	47.9	637	0.9682	5.41	166.7	11.52
342.460	2134	31.30	54.5	428	0.9913	3.22	100.7	6.59
342.502	2152	31.63	58.7	296	0.9898	3.75	118.6	7.16

Appendix II. Liquid and gas standard calibration files

Table 3. Representative liquid standard calibration file for a ~9-day interval in 2017 and their associated regression statistics and target liquid standard concentrations.

Day of Year	Slope	Intercept	R^2	Target liquid std. conc. (µmol/kg)		
117.920702	1.632	45.16	0.99937	1200	1800	2400
117.928604	1.64	32.16	0.99965	1200	1800	2400
117.93953	1.5816	76.43	0.99944	1200	1800	2400
117.947035	1.6081	39.27	0.99969	1200	1800	2400
117.971798	1.616	18.1	0.9999	1200	1800	2400
118.259087	1.6334	6.34	0.99995	1200	1800	2400
118.597431	1.6162	27.45	0.9999	1200	1800	2400
118.935835	1.6347	6.35	0.99931	1200	1800	2400
119.274005	1.6346	6.44	0.99999	1200	1800	2400
119.612327	1.6214	31.12	0.99982	1200	1800	2400
119.95059	1.6141	29.48	0.99987	1200	1800	2400
120.288901	1.6021	26.49	0.99985	1200	1800	2400
120.627147	1.6136	41.18	0.99934	1200	1800	2400
120.965532	1.6222	29.92	0.99992	1200	1800	2400
121.303837	1.6234	17.92	0.99995	1200	1800	2400
121.642229	1.605	42.06	0.99974	1200	1800	2400
121.980606	1.6174	27.17	0.99994	1200	1800	2400
122.318882	1.6114	22.82	0.99971	1200	1800	2400
122.657123	1.6075	18.87	0.9999	1200	1800	2400
122.995389	1.5946	16.51	0.99966	1200	1800	2400
123.333758	1.6046	20	1	1200	1800	2400
123.672121	1.6127	16.62	0.99988	1200	1800	2400
124.010523	1.5933	26.16	0.99994	1200	1800	2400
124.348881	1.6095	6.6	0.99982	1200	1800	2400
124.63548	1.6062	30.51	0.99962	1200	1800	2400
124.890437	1.6009	30.1	0.99995	1200	1800	2400
125.145507	1.616	14.55	0.99982	1200	1800	2400
125.400498	1.6025	28.91	0.99987	1200	1800	2400
125.65544	1.6192	22.22	0.99985	1200	1800	2400
125.846256	1.6013	44.96	0.99965	1200	1800	2400
125.883053	1.6096	35.68	0.99961	1200	1800	2400

Table 4. Representative gas standard calibration file for a ~9-day interval in 2017 and their associated regression statistics and target gas standard concentrations.

Day of Year	Slope	Intercept	R^2	Atmospheric CO_2 (ppm)	Atmospheric pressure (kPa)	Target gas std. conc. (ppmv)		
117.91334	1.0355	2.13	0.99999	408.07	102.069	1448	99.8	616
118.251726	1.0355	1.76	0.99999	437.8	102.33	1448	99.8	616
118.59007	1.0364	1.54	0.99999	427.22	102.6335	1448	99.8	616
118.928376	1.0366	1.79	0.99999	406.87	102.7865	1448	99.8	616
119.266643	1.0366	1.85	0.99999	445.52	102.594	1448	99.8	616
119.604965	1.0367	1.9	0.99999	426.55	102.436	1448	99.8	616
119.943229	1.0365	2.09	0.99999	407.09	102.273	1448	99.8	616
120.281539	1.0369	1.89	0.99999	409.09	102.1115	1448	99.8	616
120.619785	1.0369	2.31	0.99999	439.79	102.518	1448	99.8	616
120.958171	1.0378	2.11	0.99999	406.75	102.831	1448	99.8	616
121.296475	1.0374	2.2	0.99999	441.47	102.747	1448	99.8	616
121.634868	1.0374	2.3	0.99999	423.55	102.355	1448	99.8	616
121.973146	1.0378	2.1	0.99999	405.35	102.11	1448	99.8	616
122.31152	1.0373	2.09	0.99999	423.24	101.961	1448	99.8	616
122.649761	1.0377	2.23	0.99999	422.11	102.03	1448	99.8	616
122.988027	1.0386	1.82	0.99999	405.41	102.0715	1448	99.8	616
123.326397	1.0382	2.24	0.99999	423.49	102.153	1448	99.8	616
123.664759	1.0384	2.35	0.99999	407.1	102.042	1448	99.8	616
124.003161	1.0377	2.75	0.99999	401.74	101.58	1448	99.8	616
124.341519	1.0377	2.31	0.99998	404.93	101.411	1448	99.8	616
124.628118	1.0375	2.73	0.99998	407.54	101.319	1448	99.8	616
124.883075	1.0372	2.81	0.99998	405.69	101.251	1448	99.8	616
125.138146	1.0367	2.96	0.99998	404.58	100.859	1448	99.8	616
125.393137	1.0373	3.08	0.99999	406.55	100.968	1448	99.8	616
125.648078	1.0372	2.92	0.99999	407.85	101.322	1448	99.8	616
125.838894	1.0371	3.53	0.99999	407.89	101.6355	1448	99.8	616

Appendix III. Check sample inter-comparison

Triplicate check samples were taken before and after weekly servicing. 350ml amber glass bottles were triple rinsed, filled with ~1in. headspace, poisoned with 40µl $HgCl_2$, shaken vigorously, and analyzed sometime later at the OSU laboratory. While there are differences in the storage and time of analysis, variance among check samples, specifically pCO_2 values measured at the OSU lab, is likely the result of a variety of processes, namely inconsistent sampling, varying headspace volume, and transient lab conditions.

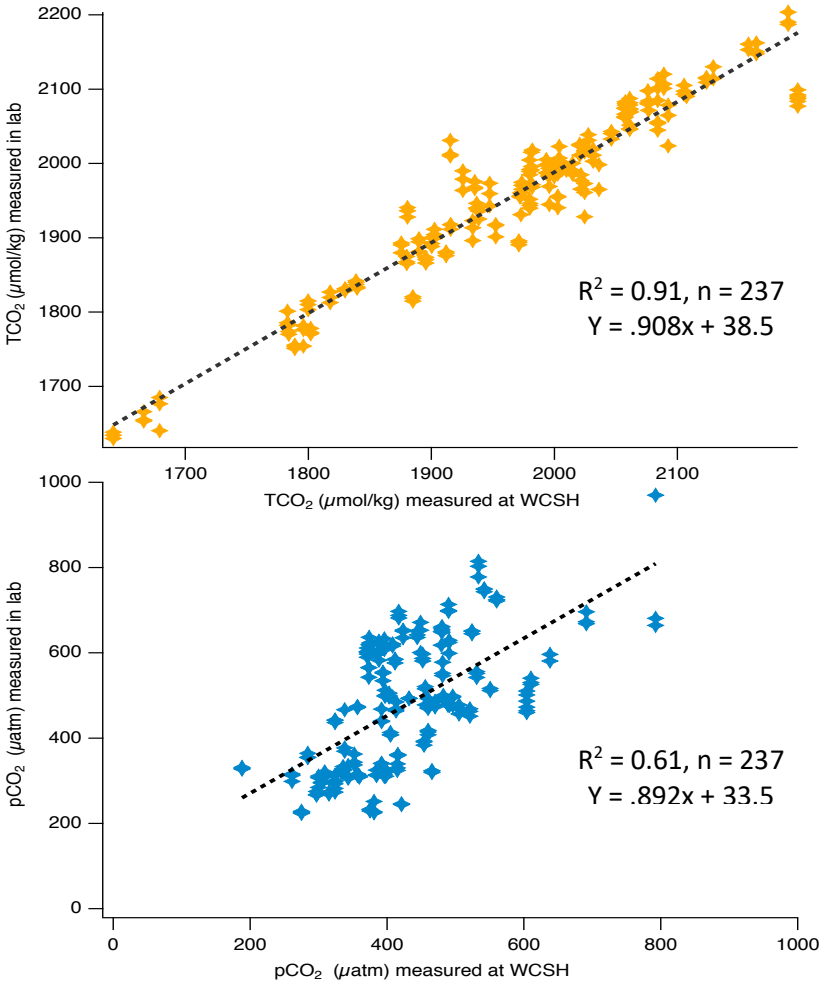

Figure 19. Comparison of TCO_2 and pCO_2 measured at WCSH with check samples measured in the OSU laboratory.

Appendix IV. Supplemental dissolved oxygen data

Beginning in late-2018, a SeaBird dissolved oxygen sensor (SBE 63) was installed upstream of the equilibration chamber and downstream of the TSG, relaying measurements in 15-second running medians. Reference salinity and temperature provided by concurrent TSG measurements relayed via LabView.

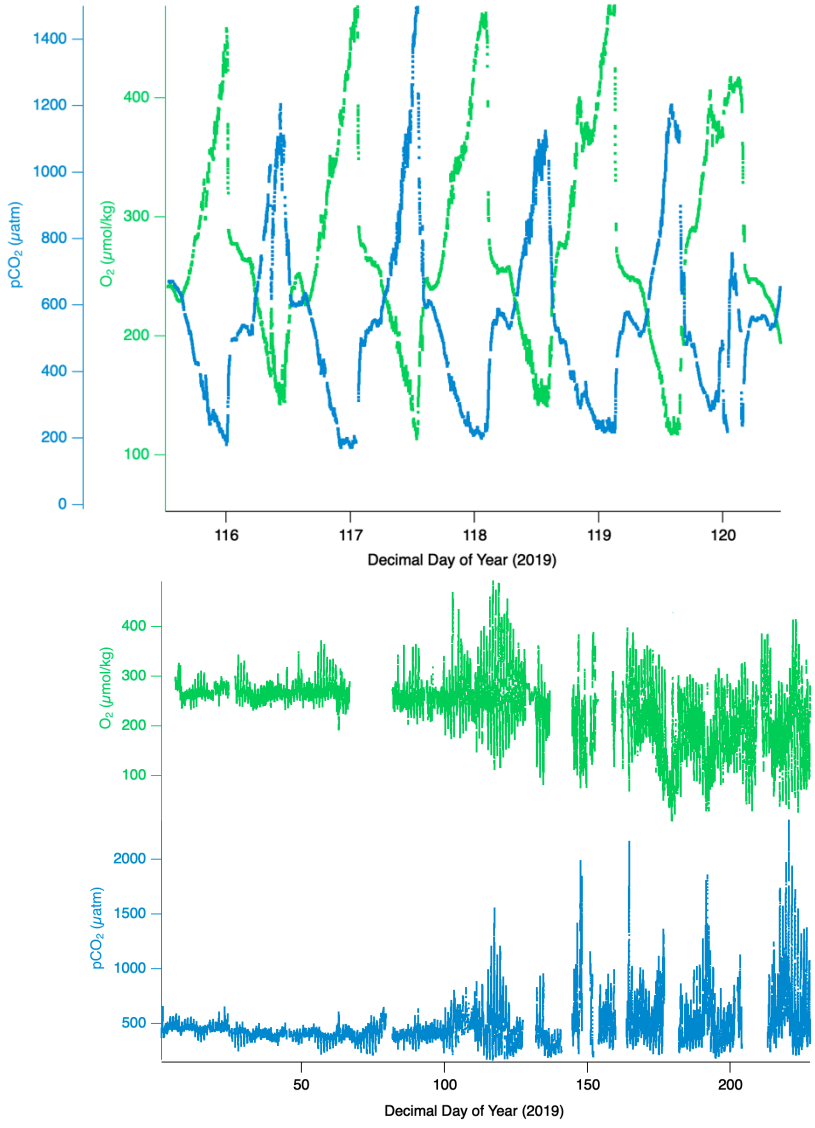

Figure 20. Dissolved oxygen (µmol/kg) and pCO_2 (µatm) for a 4-day interval in 2019 (top), and the full year's measurments of 2019 (bottom)

Appendix V. Working Code

RStudio (version 1.2.5033) was used to process QA/QC'd data files, including hourly data synchronization and implementation of the hybrid alkalinity-salinity model. The following program synchronizes data, and applies a density and CRM-correction to the TCO_2 data.

Synchronization function:

```
# This code requires:
#         - QA/QC'd monthly or annual pCO2 data file
#         - QA/QC'd monthly or annual TCO2 data file
#
# It will take hourly TCO2 measurements, find the median value
# for the last 30-seconds of the sequence, and synchronize it
# with the most recent pCO2/temp/salinity
#
# This code will output:
#         - Synchronized hourly measurements
#         - concatenated QA/QC'd pCO2 file
#         - concatenated QC/QC'd TCO2 file

rm(list=ls())
library(svDialogs); library(dplyr); library(zoo); library(purrr);

write.delim <- function(df, file, quote=FALSE, row.names=FALSE, sep='\t', ...){
  write.table(df, file,  quote=quote, row.names=row.names, sep=sep, ...)
}

# File naming
year <- as.numeric(dlgInput("Enter a year", Sys.info()["user"])$res)
sync_file <- paste("WCSH_Sync_",year,"_pCO2_TCO2",sep="")
pCO2_QC <- paste("WCSH_QC_",year,"_pCO2",sep="")
TCO2_QC <- paste("WCSH_QC_",year,"_TCO2",sep="")

# Specifying directory and output file structure
drctry = paste("~/thesis/sync_pCO2_TCO2/",year,sep="")

# Find and concatenate monthly pCO2 files
```

```
setwd(drctry)
pCO2_ls = list.files(getwd(), pattern="pCO2_smv")
pCO2_df <- lapply(pCO2_ls, function(x) {read.table(file = x, header = T, sep ="",
                                    skip                                                                    =
6,col.names=c("pCO2_DOY","pCO2","pCO2_TSG_T","pCO2_TSG_S","pCO2_Atm_CO2","pCO2_A
tm_P"),
                                    fill = TRUE)})
pCO2_df <- do.call("rbind", lapply(pCO2_df, as.data.frame))

# Find and concatenate monthly TCO2 files
setwd(drctry)
TCO2_ls = list.files(getwd(), pattern="TCO2_cnvqc")
TCO2_df <- lapply(TCO2_ls, function(x) {read.table(file = x, header = T, sep ="",
                                    skip        =        1,        col.names        =        c("TCO2_DOY",
"xCO2","xCO2_ppm","TCO2_uM_c",

"H2O_c","TCO2_TSG_T","TCO2_TSG_S","TCO2_Atm_CO2","TCO2_Atm_P","Misc"),
                                    fill = TRUE)})
TCO2_df <- do.call("rbind", lapply(TCO2_df, as.data.frame))
TCO2_df <- TCO2_df[,-c(10)]
TCO2_df[] <- lapply(TCO2_df, function(x) {as.numeric(as.character(x))})

# Filtering out NaNs
TCO2_df <- TCO2_df[complete.cases(TCO2_df),]
pCO2_df <- pCO2_df[complete.cases(pCO2_df),]

# xTCO2 -> TCO2(umol/kg) density conversion:
# Using the Sea Water Density UNESCO Formula:
# https://link.springer.com/content/pdf/bbm%3A978-3-319-18908-6%2F1.pdf

K <- TCO2_df$TCO2_TSG_T; S <- TCO2_df$TCO2_TSG_S

# Seawater thermodynamic constants given T,S,P
a0 = 999.842594; a1 = 6.793953e-2; a2 = -9.095290e-3; a3 = 1.001685e-4;
a4 = -1.120083e-6; a5 = 6.536332e-9
b0 = 8.2449e-1; b1 = -4.0899e-3; b2 = 7.6438e-5; b3 = -8.2467e-7; b4 = 5.3875e-9
c0 = -5.7246e-3; c1 = 1.0227e-4; c2 = -1.6546e-6
d0 = 4.3814e-4

# Apply UNESCO formula
TCO2_df$p_sample <- a0 + a1*K + a2*K^2 + a3*K^3 + a4*K^4 + a5*K^5 +
  S*(b0 +b1*K + b2*K^2 + b3*K^3 + b4*K^4) + (S^1.5)*(c0 + c1*K + c2*K^2) + (S^2)*(d0)
TCO2_df$p_std <- rep(1000.16, nrow(TCO2_df))
```

```
# Apply CRM-correction
TCO2_df$TCO2_umol_kg <- TCO2_df$TCO2_uM_c*(TCO2_df$p_std /
TCO2_df$p_sample)*0.985 #density and CRM correction
TCO2_df <- TCO2_df[,-c(2,3,10,11)]

# Filtering out NaNs and fliers
TCO2_df$TCO2_umol_kg[TCO2_df$TCO2_umol_kg < 0] <- NaN
TCO2_df <- TCO2_df[complete.cases(TCO2_df),]

# Syncing the QAQC'd pCO2 with density + CRM-corr'd TCO2 by timestamp
Sync_df <- merge(pCO2_df,TCO2_df, by.x = 1, by.y = 1, all=TRUE)
Sync_df[is.na(Sync_df)] <- "NaN"
Sync_df <- as.data.frame(sapply(Sync_df, as.numeric))

# Create empty vectors
TCO2_DOY = c(); pCO2_uatm = c(); Atm_CO2 = c(); Atm_P = c();
TCO2_umol_kg = c(); TCO2_T = c(); TCO2_S = c();

# Loop row-wise through sync'd data to locate and then interpolate pCO2 values:
for(i in 1:(nrow(Sync_df))) {

  if(!is.na(Sync_df$pCO2[i]) && !is.na(Sync_df$TCO2_umol_kg[i+1])) {

    # Find index when TCO2 switches back to pCO2
    NonNAindex <- which(is.na(Sync_df$TCO2_umol_kg[(i+1):(i+500000)]))
    idx <- min(NonNAindex)
    idx = idx + i

    # Apply index and find median TCO2/T/S/DOY and interp pCO2
    TCO2_DOY[i] <- median(Sync_df$pCO2_DOY[(i+30):(idx-1)], na.rm=T)
    TCO2_umol_kg[i] <- median(Sync_df$TCO2_umol_kg[(i+30):(idx-1)], na.rm=T)
    TCO2_T[i] <- median(Sync_df$TCO2_TSG_T[(i+30):(idx-1)], na.rm=T)
    TCO2_S[i] <- median(Sync_df$TCO2_TSG_S[(i+30):(idx-1)], na.rm=T)
    pCO2_uatm[i] <- Sync_df$pCO2[i] + ((Sync_df$pCO2[idx] - Sync_df$pCO2[i])/
                                Sync_df$pCO2_DOY[idx] - Sync_df$pCO2_DOY[i])*
                               (Sync_df$pCO2_DOY[idx] - TCO2_DOY[i])
  }
}

# Creating sync dataframe
sync <- data.frame(TCO2_DOY, pCO2_uatm, TCO2_umol_kg, TCO2_S, TCO2_T)
sync <- sync[complete.cases(sync),]

# Create empty vectors
```

```
TCO2_DOY_ = c(); Atm_CO2_ = c(); Atm_P_ = c();TCO2_umol_kg_ = c(); TCO2_T_ = c(); TCO2_S_ = c();

for(i in (1+179):(nrow(TCO2_df)-1)){

  # Create a QC TCO2 data frame
  if((TCO2_df$TCO2_DOY[i+1] - TCO2_df$TCO2_DOY[i] > 0.02) &&
     (TCO2_df$TCO2_DOY[i+1] - TCO2_df$TCO2_DOY[i] < .25)){

      # Apply index and find median TCO2/T/S/DOY and interp pCO2
      TCO2_DOY_[i] <- median(TCO2_df$TCO2_DOY[(i-180):(i)], na.rm=T)
      TCO2_umol_kg_[i] <- median(TCO2_df$TCO2_umol_kg[(i-180):(i)], na.rm=T)
      TCO2_T_[i] <- median(TCO2_df$TCO2_TSG_T[(i-180):(i)], na.rm=T)
      TCO2_S_[i] <- median(TCO2_df$TCO2_TSG_S[(i-180):(i)], na.rm=T)

     }
}

# Creating QC TCO2sync dataframe
TCO2_QC_df <- data.frame(TCO2_DOY_, TCO2_umol_kg_, TCO2_T_, TCO2_S_)
TCO2_QC_df <- TCO2_QC_df[complete.cases(TCO2_QC_df),]

# Add header information
writeLines(c("3 header lines","Synchronized WCSH pCO2/TCO2","DOY pCO2_uatm TCO2_umol_kg TSG_S TSG_T"), sync_file)
writeLines(c("3 header lines","QA/QC smooth WCSH pCO2","DOY pCO2 TSG_T TSG_S Atm_CO2 Atm_P"), pCO2_QC)
writeLines(c("3 header lines","QA/QC smooth WCSH TCO2","DOY TCO2 TSG_T TSG_S"), TCO2_QC)

# Write to dat file
write.delim(sync, sync_file, row.names=F, col.names=F, quote=F, sep="\t", append=T) # Write to dat file
write.delim(pCO2_df, pCO2_QC, row.names=F, col.names=F, quote=F, sep="\t", append=T) # Write to dat file
write.delim(TCO2_QC_df, TCO2_QC, row.names=F, col.names=F, quote=F, sep="\t", append=T) # Write to dat file
```

Synchronized pCO_2/TCO_2 data files are then fed through CarbCalc to calculate relevant carbonate variables: pH, alkalinity, and saturation state. The following program ingests output from CarbCalc to perform running 6-hour alkalinity-salinity regressions (at minimum) and returns a data-frame containing slope, intercept, and a variety of useful statistics (R^2, average deviation, etc). The output of this program is fed into the hybrid alkalinity-salinity program to resolve variable carbonate parameters at the high-resolution pCO_2 product.

Alkalinity-salinity regression function:

```
rm(list=ls())

library(zoo); library(dplyr); library(tidyr); library(ggplot2)
library(foreign); library(readr); library(nlme); library(magrittr); library(svDialogs);

write.delim <- function(df, file, quote=FALSE, row.names=FALSE, sep='\t', ...){
  write.table(df, file,  quote=quote, row.names=row.names, sep=sep, ...)
}

lsqfitx <- function(X,Y){

  # This function is taken from Edward T Peltzer, MBARI
  # The line is fit by minimizing the residuals of the X only
  #
  # The equation of the line is Y = mx*X + bx
  #
  # Equations from Bevington & Robinson (1992)
  # Data Reduction and Error Analysis for the Physical Sciences, 2nd Ed
  # pp 104, 108-109

  # X = x data; Y = y data

  # mx = slope; bx = y-intercept
  # rx = correlation coefficient
  # smc = std. dev of the slope; sbx = std dev of the y-intercept
```

```
  # Find length of data
  n = length(X)

  # Calculate the sums
  Sx = sum(X); Sy = sum(Y); Sx2 = sum(X^2); Sxy = sum(X*Y); Sy2 = sum(Y^2)

  # Find numerator and denominator
  num = (n*Sxy) - (Sy*Sx)
  den = (n*Sy2) - (Sy)^2

  # Calculate m, a, rx, s2, sm, and sb
  mxi = num/den
  a = (Sy2*Sx - Sy*Sxy)/den
  rx = num/(sqrt(den)*sqrt(n*Sx2-Sx^2))

  diff =  X - a - mxi*Y

  s2 = sum(diff*diff)/(n-2)
  sm = sqrt(n*s2/den)
  sa = sqrt(Sy2*s2/den)

  #Transpose coefficients
  mx = 1/mxi; bx = -a/mxi

  # Find slope and intercept
  smx = mx*sm/mx; sbx = abs(sa/mxi)

  return(list(mx,bx,rx,smx,sbx)
}

lsqfity <- function(X,Y){
   # This function is taken from Edward T Peltzer, MBARI
  # The line is fit by minimizing the residuals of the Y only
  #
  # The equation of the line is Y = mx*X + by
  #
  # Equations from Bevington & Robinson (1992)
  # Data Reduction and Error Analysis for the Physical Sciences, 2nd Ed
  # pp 104, 108-109

  # X = x data; Y = y data

  # my = slope; by = y-intercept
  # ry = correlation coefficient
```

```
  # smy = std. dev of the slope; sby = std dev of the y-intercept

  # Find length of data
  n = length(X)

  # Calculate the sums
  Sx = sum(X); Sy = sum(Y); Sx2 = sum(X^2); Sxy = sum(X*Y); Sy2 = sum(Y^2)

  # Find numerator and denominator
  num = (n*Sxy) - (Sx*Sy); den = (n*Sx2) - (Sx)^2

  # Calculate my, by, ry, s2, smy, and sby
  my = num/den
  by = (Sx2*Sy - Sx*Sxy)/den
  ry = num/(sqrt(den)*sqrt(n*Sy2-Sy^2))

  diff =  Y - by - my*Y

  s2 = sum(diff*diff)/(n-2)
  smy = sqrt(n*s2/den); sby = sqrt(Sx2*s2/den)

  fity <- c(my,by,ry,smy,sby)
  return(fity)
}

lsqbisec <- function(X,Y){
  # This function is taken from Edward T Peltzer, MBARI
  # The slope of the line is determined by calculating the slope
  # of the line that bisects the minor angle between the
  # regression of Y-on-X and X-on-Y

  # Referred to as the LEAST SQUARES BISECTOR

  #
  # The equation of the line is y = mx+b
  #
  # Equations from Bevington & Robinson (1992)
  # Data Reduction and Error Analysis for the Physical Sciences, 2nd Ed
  # pp 104, 108-109

  # X = x data; Y = y data

  # m = slope; y = y-intercept
  # r = correlation coefficient
```

```
# sm = std. dev of the slope; sb = std dev of the y-intercept

my <- lsqfity(X,Y)
my <- as.numeric(my[1])

mx <- lsqfitx(X,Y)
mx <- as.numeric(mx[1])

# Calculate least sqaures bisector slope
theta = (atan(my) + atan(mx))/2
m = tan(theta)

# Determine size of the vector
n = length(X)

# Calculate the sums
Sx = sum(X); Sy = sum(Y)
xbar = Sx/n; ybar = Sy/n

# Calculate least squares bisector intercept
b = ybar - m * xbar

# More sums
Sxy = sum(X*Y); Sx2 = sum(X^2)

# Calculate reused expression
den = n*Sx2 - Sx^2

# Calculate r, sm, sb, s2
r = sqrt(my/mx)

 if(my < 0 && mx < 0){
   r = -r
 }

diff = Y - b - m*X

s2 = sum(diff*diff)/(n-2)
sm = sqrt(n*s2/den)
sb = sqrt(Sx2*s2/den)

fitbisec <- c(m,b,r,sm,sb)
return(fitbisec)
```

```
}

year <- as.numeric(dlgInput("Enter a year", Sys.info()["user"])$res)
load_file = paste("Sync_carb_param_",year,".txt",sep="")
out_file = paste("WCSH_",year,"_","AlkS", sep="")
drctry = paste("~/desktop/thesis/Sync_Alk_pH_om/",sep="")

setwd(drctry)
AlkS_ls = list.files(getwd(), pattern=load_file);
AlkS_df <- lapply(AlkS_ls, function(x) {read.table(file = x, header = T, sep ="", skip = 1, col.names
=
c("Alk","TCO2","pCO2","CO2","HCO3","CO32","pH","omega_c","omega_a","DOY","Sal","Temp"
), fill = TRUE)});
AlkS_df <- do.call("rbind", lapply(AlkS_df, as.data.frame))

# Create empty arrays
DOY = c(); m = c(); b = c(); r_sqrd = c(); Alk_ref = c(); S_ref = c(); m_dev = c(); b_dev = c(); num =
c();
avg_dev = c(); avg_abs_dev = c(); avg_sq_dev = c(); rms = c(); DOY_i = c(); DOY_f = c();

n = 6    # minimum number of points to regress

for (i in 1:(nrow(AlkS_df)-6)){

  if(((AlkS_df$DOY[i+n] - AlkS_df$DOY[i]) <= 2)){

      # Calculate reference sal and alk
      S_ref[i] <- mean(AlkS_df$Sal[(i):(i+n)]);
      Alk_ref[i] <- mean(AlkS_df$Alk[(i):(i+n)]);
      X <- (AlkS_df$Sal[(i):(i+n)]);
      Y <- (AlkS_df$Alk[(i):(i+n)]);

      # Apply regression
      bisec <- lsqbisec(X,Y);

      # Append to array
      DOY[i] <- mean(AlkS_df$DOY[(i):(i+n)]);
      DOY_i[i] <- head(AlkS_df$DOY[i], n=1);
      DOY_f[i] <- tail(AlkS_df$DOY[i+n-1], n=1);

      # Fetch slope, int, rsq, m_dev, b_dev, number of iterations
      m[i] <- bisec[1]; b[i] <- bisec[2];
      r_sqrd[i] <- bisec[3]; m_dev[i] <- bisec[4];
      b_dev[i] <- bisec[5]; num[i] <- n;
```

```
      # Calculate other regression statistics
      avg_dev[i] <- ((m[i] %*% X + b[i]) - Y)/num[i]; # model-observation
      avg_abs_dev[i] <- mean(abs((bisec[1]*X + bisec[2]) - Y));
      avg_sq_dev[i] <- mean(((bisec[1]*X + bisec[2]) - Y)^2);
      rms[i] <- (1/n) * sqrt(((bisec[1]*X + bisec[2]) - Y)^2);
      alk_fw_unct[i] <- sqrt((b_dev[i])^2 + (m_dev[i] * S_ref[i]^2));

    # Reset n
    n=5;

  }

  # Move forward one row
  n=n+1;

}

# Create dataframe
AlkS_regress <- data.frame(DOY, DOY_i, DOY_f, Alk_ref, S_ref, m, b, r_sqrd, m_dev, b_dev,
num, avg_abs_dev)

# Filter out fliers
AlkS_regress$avg_abs_dev[AlkS_regress$avg_abs_dev > 35] <- NaN
AlkS_regress$m_dev[AlkS_regress$m_dev > 100] <- NaN
AlkS_regress$m[AlkS_regress$m > 500 | AlkS_regress$m < 0] <- NaN
AlkS_regress$b[AlkS_regress$b > 1000 | AlkS_regress$b < -200] <- NaN
AlkS_regress <- na.omit(AlkS_regress)

# Write to dat file
write.delim(AlkS_regress, out_file, row.names=FALSE, quote=FALSE, sep="\t") # Write to dat
file
```

Hourly alkalinity-salinity slope and intercept produced in the prior program allows calculation of alkalinity at the same resolution as the high-resolution pCO_2 data product. Then, TCO_2, pH, and saturation state can be calculated for subhourly intervals in-between hourly TCO_2 analysis. The end product is a full-resolution suite of carbonate variables at the same 30-second resolution of pCO_2 analysis.

Alkalinity-salinity interpolation function:

```
rm(list=ls())

library(svDialogs); library(dplyr)

write.delim <- function(df, file, quote=FALSE, row.names=FALSE, sep='\t', ...){
  write.table(df, file,  quote=quote, row.names=row.names, sep=sep, ...)
}

year <- as.numeric(dlgInput("Enter a year", Sys.info()["user"])$res)
AlkS_file = paste("WCSH_",year,"_AlkS",sep="")
pCO2_file = paste("WCSH_QC_",year,"_pCO2", sep="")
out_file_1 = paste("WCSH_",year,"_","AlkS_carbcalc", sep="")
out_file_2 = paste("WCSH_",year,"_","AlkS_interp", sep="")

# Search for ALkS file
drctry = "~/desktop/Thesis/AlkS"
setwd(drctry) # Search for the AlkS file containing all sync'd Alk values
AlkS_ls = list.files(getwd(), pattern=AlkS_file);
AlkS_df <- lapply(AlkS_ls, function(x) {read.table(file = x, header = T, sep ="", skip = 1)});
AlkS_df <- do.call("rbind", lapply(AlkS_df, as.data.frame))
colnames(AlkS_df) <- c("DOY","DOY_i", "DOY_f", "Alk_ref", "S_ref", "m", "b", "r_sqrd",
"m_dev", "b_dev","num","avg_abs_dev")

# Search for annual pCO2 file
drctry = paste("~/desktop/Thesis/Sync_pCO2_TCO2/",year,sep="")
setwd(drctry) # Search for QC/QA pCO2 file
pCO2_ls = list.files(getwd(), pattern=pCO2_file);
pCO2_df <- lapply(pCO2_ls, function(x) {read.table(file = x, header = T, sep ="", skip = 3)});
```

```
pCO2_df <- do.call("rbind", lapply(pCO2_df, as.data.frame))
colnames(pCO2_df) <- c("DOY","pCO2", "TSG_T", "TSG_S", "Atm_CO2", "Atm_P")

# Interpolation function using only the synchronized values (df = AlkS_c_df)
AlkS_interp <- function(AlkS_df, pCO2_df, DOY_pCO2, DOY_m, pCO2_S, pCO2_T, pCO2, m, b){
    for (i in 1:(nrow(AlkS_df)-1)){
      for(j in 1:(nrow(pCO2_df))){
           if(DOY_pCO2[j] >= DOY_m[i] && DOY_pCO2[j] <= DOY_m[i+1] &&
            (DOY_m[i+1] - DOY_m[i] < 1)){

            DOY_[j] <- DOY_pCO2[j];
            TSG_T[j] <- pCO2_T[j];
            TSG_S[j] <- pCO2_S[j];
            pCO2_[j] <- pCO2[j];
            m_[j] <- m[i] + ((DOY_pCO2[j]-DOY_m[i])/(DOY_m[i+1]-DOY_m[i]))*(m[i+1]-m[i])
            b_[j] <- b[i] + ((DOY_pCO2[j]-DOY_m[i])/(DOY_m[i+1]-DOY_m[i]))*(b[i+1]-b[i])
           }
        }
    }
 return(list(DOY_, pCO2_, TSG_T, TSG_S, m_, b_))
}

# Create emtpty arrays
Alk_ = c(); pCO2_ = c(); TSG_T = c(); TSG_S = c(); DOY_ = c(); m_ = c(); b_ = c();

# Execute function
AlkS_interp_df <- (AlkS_interp(AlkS_df, pCO2_df, pCO2_df$DOY, AlkS_df$DOY,pCO2_df$TSG_S,
                        pCO2_df$TSG_T, pCO2_df$pCO2,AlkS_df$m, AlkS_df$b))

AlkS_interp_df <- as.data.frame(AlkS_interp_df)
colnames(AlkS_interp_df) <- c("DOY","pCO2","TSG_T","TSG_S","m","b")
AlkS_interp_df[is.na(AlkS_interp_df)] <- NaN
AlkS_interp_df <- na.omit(AlkS_interp_df)

# Calculate AlkS
AlkS_interp_df$AlkS <- AlkS_interp_df$TSG_S*AlkS_interp_df$m + AlkS_interp_df$b

write.delim(AlkS_interp_df, out_file_2, row.names=FALSE, quote=FALSE, sep="\t") # Write to
dat file
```

Appendix VI. Data processing

Data processing represented a primary challenge for the duration of this study. The likelihood of system malfunction, be it from computer failure, LiCOR detector failure, or simply power outages is inevitable across six years of continuous sampling. This appendix will layout the most common problems we encountered during sample collection and data processing.

Figure 21 shows raw uncalibrated xCO_2, salinity, and temperature for January of 2018. The system behaves normally from day 0-4, until there is a large negative departure in

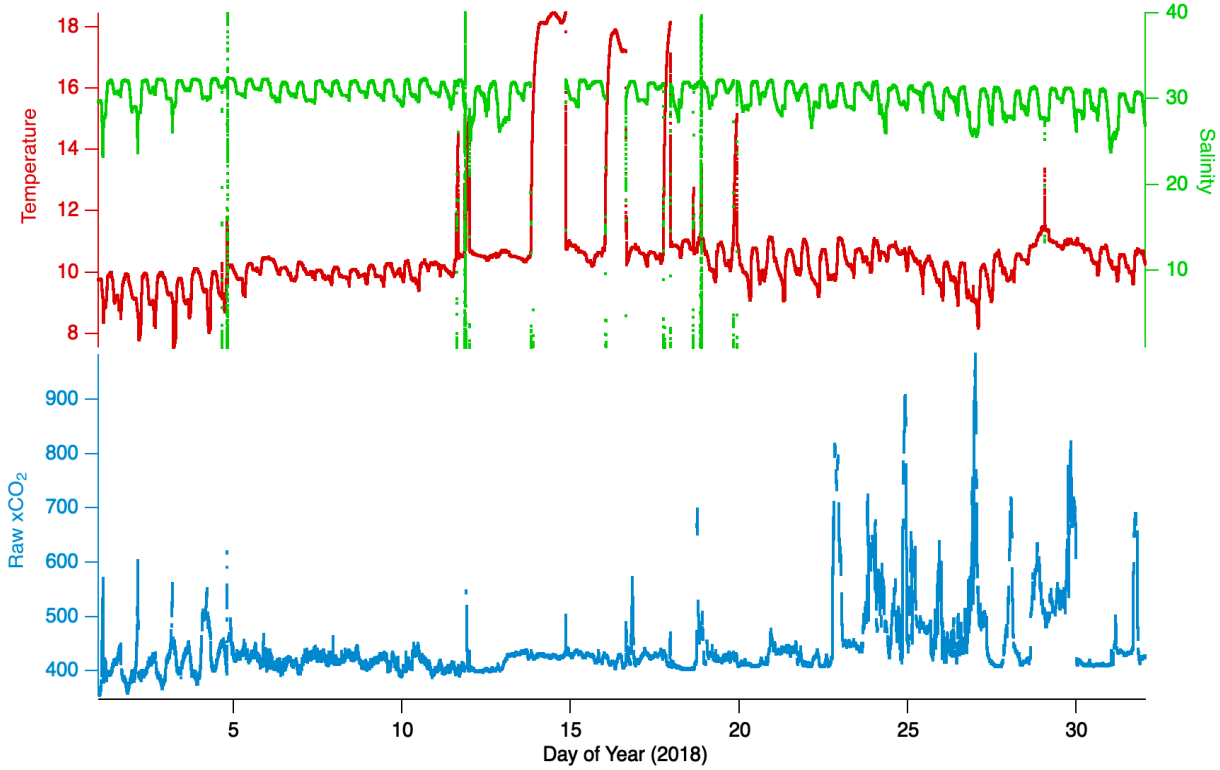

Figure 21. Raw xCO_2 (blue line), temperature (red line), and salinity (green line) for January 2018.

salinity and noisy xCO_2 data that doesn't resemble any of the diel or tidal characteristics observed for any part of the study. The spikes in salinity occurring on day 5, 13, 14, 16, and 18-20 are signatures of no liquid flow through. Hatchery workers routinely shut off flow to clean pipes which results in flow to the instrument to be shut off. If the instrument is not placed into "wait mode" it will continue recording temperature, salinity, and pCO_2 data. The large negative salinity departures are a result of the TSG measuring an emptying pipe. With flow off, the pipes warm up to ambient room air, resulting in a distinct asymptotic temperature signal. As the equilibration chamber warms up, pCO_2 increases steadily, resulting in a slow-building pCO_2 signal as well. For this interval in 2018, the flow is stopped several times throughout the month, and is off for all of day 14. When flow is reestablished, salinity and temperature return to their distinct tidally influenced signal commonly observed in the winter months.

Trickier to diagnose from flow stoppage is ambient room air leaking into the equilibration chamber. Usually a leak to atmosphere means the recirculating air loop is blocked—likely from a water source. Simply follow the air-loop pathway and dislodge the rogue trapped water. A quick way to test this in person is by exhaling near the equilibration chamber and observing the response: within ~20 seconds you should observe a rapid spike up followed by a gradual sloping back down to atmospheric CO_2 levels. From day 5-30, there was a clear leak to atmosphere in addition to a handful of liquid flow stoppage. Sadly, none of this pCO_2 data is useful and has to be masked out during post-processing.

Figure 22 shows standard-converted but not yet QA/QC'd hourly TCO_2 data for a ~3 days in 2018. There is a ~2 minute response time transitioning from pCO_2 mode to TCO_2

mode. We simply mask out these two minutes and find a running median of the final 30 seconds. If the HCl runs out, the TCO_2 response falls to zero. Occasionally replacing the pump seal will help to reduce a noisy TCO_2 response.

Following the TCO_2 analysis, the system transitions back into high-resolution continuous pCO_2. This response time is determined in part by ensuring sure the air-path is unobstructed and that a clean aerosol inlet filter is routinely replaced. The program developed to compile raw data allows the user to mask out this transitory step by determining the length of time needed for full equilibration. For this study, the masking times varied from 60 seconds to several minutes. Figure 23 demonstrates the raw xCO_2 signal (red) and the transition-masked quality-controlled xCO_2 product.

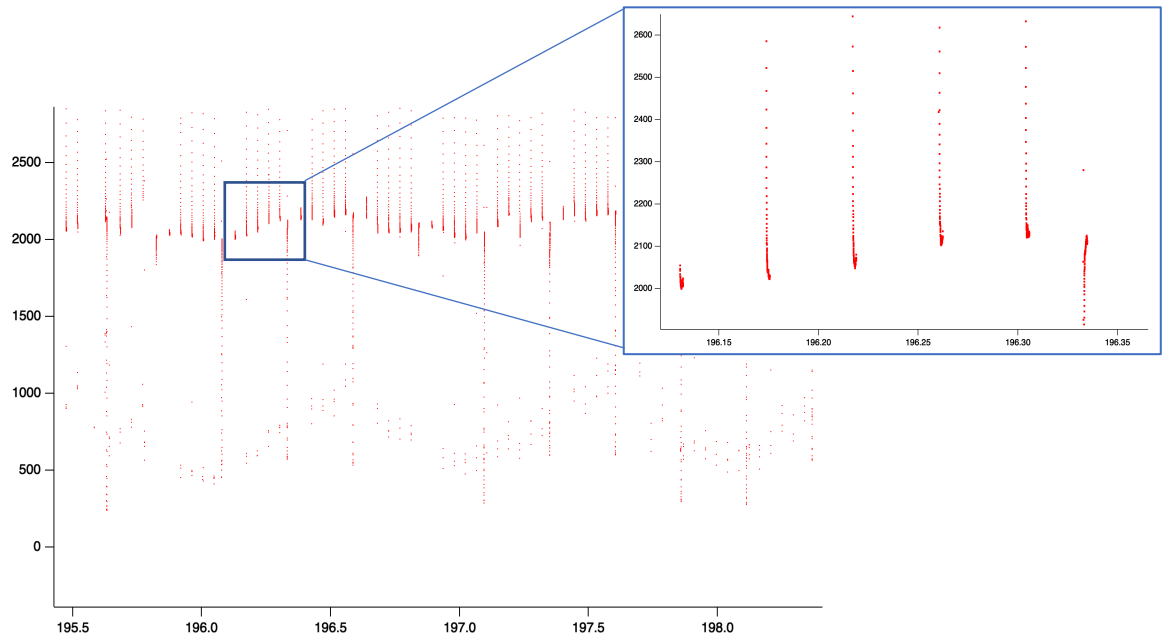

Figure 22. Non QA/QC'd TCO_2 data from a three-day period of 2018.

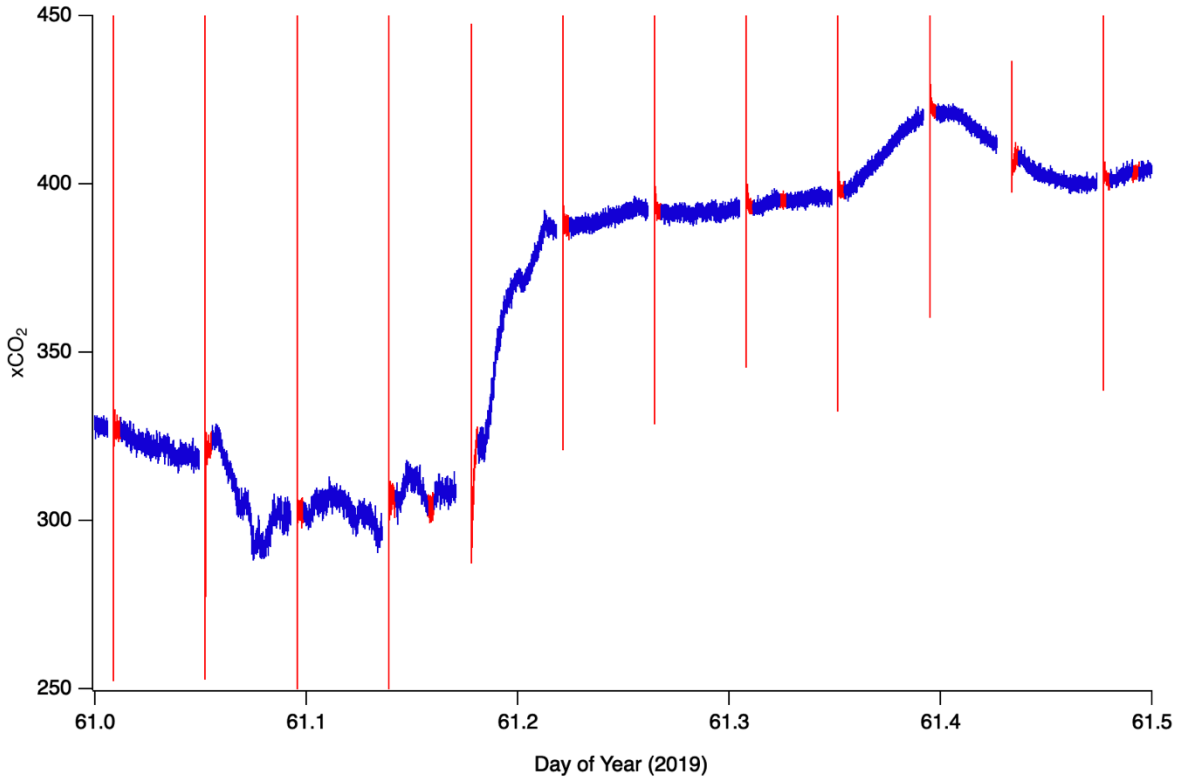

Figure 23. xCO_2 for a half-day interval of 2019 demonstrating the raw signal (red) and the transition-masked xCO_2 in blue.

Appendix VII. Data access

Acquisition of data presented within the scope of this research will be made available upon request. Please contact fairchiw@oregonstate.edu or burke.hales@oregonstate.edu for further details.